PHYSICS EDUCATION

Quarterly e-journal dedicated to Physics Pedagogy

Vol. 40, Issue 2 | April–June 2026

In This Issue:

PHYSICS EDUCATION

Vol. 40, Issue 2 | April-June 2026 | Editorial

Bridging Theory, Experiment, and Epistemology in Modern Physics Pedagogy

Evolution of Learning Frameworks in the Digital Age

As physics education moves deeper into the twenty-first century, the interface between how students conceptualize physical laws and how they practice scientific inquiry undergoes continuous transformation. Physics pedagogy is no longer confined to the standard exposition of analytical formulas or the mechanical execution of laboratory recipes. Instead, modern physics education demands a holistic ecosystem where epistemological beliefs, statistical rigor, laboratory innovations, and advanced computational techniques converge to build robust cognitive models. The current issue of *Physics Education* (Volume 40, Issue 2) serves as a testament to this convergence, highlighting diverse methodologies that redefine undergraduate and postgraduate learning environments.

A foundational pillar of active learning rests on understanding how students view knowledge itself. Epistemological beliefs—questions regarding whether physics knowledge is an accumulation of isolated facts given by authority or a coherent, evolving framework constructed through evidence—fundamentally dictate student engagement. When educators actively cultivate sophisticated epistemological views, students transition from passive memorization to authentic physics reasoning. This shift influences not only their problem-solving heuristics but also their willingness to navigate the inherent cognitive dissonance that accompanies complex subjects like quantum mechanics or statistical thermodynamics.

> *"True physics pedagogy bridges the gap between the pristine mathematical structures of theory and the inherently noisy, chaotic domain of real-world observations."*

Parallel to cognitive framework adjustments is the necessity for technical and methodological discipline in the laboratory. Quantitative experimental literacy requires more than noting observations down in a logbook; it requires a deep statistical understanding of experimental boundaries. A critical question facing undergraduate researchers is determining the empirical threshold of data—specifically, how many trials are statistically sufficient to confidently isolate a signal from noise or to validate a physical constant? Providing students with a structured statistical approach to trial optimization addresses a perennial gap in laboratory training, shifting focus from arbitrary replication to data-driven validation.

Furthermore, expanding technological access makes it possible to introduce advanced experimental frameworks early in higher education. Holography, long considered an advanced optical specialization, can be seamlessly integrated into undergraduate laboratories through systematic recording and reconstruction protocols. Such hands-on encounters with wavefront reconstruction compress the distance between abstract classical electrodynamics and concrete optical engineering, giving students direct experience with visual spatial coherence.

Simultaneously, computational physics continues to bridge gaps where analytic treatments fail. The double pendulum, a classic emblem of complex mechanics, comes alive when paired with magnetic damping, numerical simulations, and chaos characterization. Exposing students to computational phase space modeling transforms chaos from an abstract phrase into a vivid, visual demonstration of sensitive dependence on initial conditions.

Finally, as cutting-edge informatics integrates with physical models, introducing contemporary paradigms like Reservoir Computing for time-series predictions ensures that students remain at the frontier of applied physics. By understanding how recurrent neural networks exploit physical or simulated dynamical systems to project complex data, physics graduates are uniquely equipped to navigate an increasingly data-dense scientific landscape. We trust that the diverse insights compiled in this issue will inspire educators to refine their pedagogical toolkits and continue fostering scientific curiosity.

Editorial Team

Exploring the Role of Epistemological Beliefs in Shaping Teaching and Learning Practices

Sapna Sharma[1] and P. K. Ahluwalia[2]

[1]Department of Physics, St. Bede's College, Shimla 171002, India.
[2]Department of Physics, Himachal Pradesh University, Shimla 171005, India.

Submitted on 25-09-2025
Accepted on 13-04-2026

Abstract

Learning strategies and instructional practices are greatly influenced by epistemological views, which are ideas about the nature of knowledge and knowing. Students' learning techniques and learning outcomes are shaped by teachers' instructional practices, which are influenced by their epistemological ideas, as research has repeatedly shown. These ideas have an impact on students' comprehension of the material and are strongly related to their engagement, motivation, and future academic and professional paths. In this study, the epistemological beliefs of physical science teachers were investigated using the Epistemological Beliefs Assessment for Physical Science (EBAPS) survey instrument. Data were collected from four distinct groups of teachers (N = 173): three groups teaching at different types of schools (privately managed school, centrally administered public school, and state run government school) and one group teaching undergraduate (UG) and postgraduate (PG) college courses. In addition, undergraduate students (N = 86) from two colleges in Shimla, India, were included in the study. A preliminary examination of the gathered data is presented in this study. The findings show that neither the two undergraduate student groups nor any of the four teacher groups had extremely advanced or expert-like epistemic viewpoints. This emphasizes the necessity to explicitly address epistemological beliefs in teaching physical science. Differences observed between teachers and students' epistemological orientations suggest that instructional practices, curricular materials, and assessment structures may implicitly reinforce procedural and authority-driven perspective of scientific knowledge. In addition, the study explores how teachers' epistemological beliefs vary across gender and levels of teaching experience, contributing to a more nuanced understanding of epistemic orientations among science educators. The study underscores the need for teacher education and professional development programs to engage with epistemological dimensions of teaching and learning, and provides empirical evidence from an underrepresented Indian

context, contributing to broader discussions on epistemic development in science education.
keywords Epistemological beliefs, concept survey, learner-centered

1 Introduction

In Indian classrooms, the pressure to complete a prescribed syllabus within a limited timeframe often compels teachers to prioritize rapid content delivery. Because of this, classroom instruction often becomes teacher-centered, with students positioned as passive recipients and teachers serving as the main source of knowledge. Students' pre-existing beliefs, assumptions, and perspectives about knowledge and learning are largely ignored in such instructional settings, where the assessment of students' prior understanding is typically limited to academic performance or examination scores. However, learning is a constructive process that is heavily impacted by learners' epistemological beliefs that is, their views about the nature of knowledge, knowing, and learning rather than just the accumulation of factual information. Research has consistently shown that meaningful learning occurs when new information is connected with learners' prior knowledge and their epistemological beliefs [1–2]. When students perceive scientific knowledge as fixed, certain, and transmitted by authority, they are less likely to engage in inquiry, critical thinking, or conceptual change. Conversely, students who view knowledge as evolving and justified through evidence are more likely to adopt deeper learning strategies and develop scientific reasoning skills. While considerable attention has been paid to teachers' epistemological beliefs, students' epistemological beliefs are equally important, particularly in the Indian educational context where examination-oriented practices dominate classroom culture. Students' beliefs about whether scientific ability is innate or improvable, whether knowledge is absolute or tentative and whether learning requires memorization or understanding directly influence how they approach learning tasks, respond to instruction, and engage with scientific concepts. Ignoring these beliefs may limit the effectiveness of pedagogical reforms aimed at promoting inquirybased and learner-centered science education. Several studies [3–4] have examined science teachers' epistemological beliefs and have provided substantial evidence that these beliefs significantly influence classroom practices [5–8]. Teachers' beliefs play a crucial role in shaping instructional goals and in determining how these goals are translated into lesson planning and classroom implementation [9–10]. It has been suggested that teachers holding constructivist epistemological beliefs are more capable of identifying students' alternative conceptions and addressing them effectively than teachers with empiricist beliefs [11]. In the context of on-going educational reforms, particularly those emphasizing conceptual understanding and scientific reasoning, attending to teachers' epistemological beliefs becomes essential, as these beliefs serve as a strong indicator of the nature and quality of classroom practices [12]. At the same time, examining students' epistemological beliefs alongside those of teachers provides a more comprehensive understanding of classroom dynamics and learning outcomes [13-18]. Such an approach is particularly relevant in the context, where diverse classroom settings, examination-oriented practices, and varying levels of exposure to inquiry-based learning often create a disconnect between teachers' instructional beliefs and students' learning beliefs, thereby significantly influencing students' engagement with science and their development as scientific thinkers. Several surveys have been created to assess the impact of epistemological beliefs on learning. These include the MPEX survey developed by Redish et al. [19], the VASS by Halloun and Hestenes [20], and the CLASS by Adams et al. [21]. These surveys are commonly referred to as attitude or affective surveys. In contrast, the Epistemological Beliefs Assessment for Physical Science Survey (EBAPS) by Elby et al. [22] specifically targets views and concepts related to the physical sciences. While numerous studies have explored teachers' beliefs and instructional approaches in Western contexts, empirical research in the Indian educational landscape remains scarce. Research on epistemology in science education has highlighted the role of learners' and teachers' beliefs about knowledge, knowing, and knowledge construction in shaping learning processes and instructional practices [23-24]. In the context of the physical sciences, epistemological constructs have been examined through various frameworks. Research on epistemological beliefs in the Indian physical sciences is limited but growing. Sharma, Ahluwalia, and Sharma (2013) examined both students' and teachers' beliefs in physics using the MPEX survey, finding that students often hold transitional or naïve beliefs emphasizing memorization, while teachers display a mixture of sophisticated and traditional orientations [25]. Sen and Karwande (2025) explored higher education teachers' epistemological beliefs, showing that although many teachers value conceptual understanding, classroom practices do not always reflect these beliefs [26]. Additional work from the epiSTEME conference series highlights epistemic practices in Indian science classrooms [27]. Despite these contributions, studies rarely examine teachers and students together or adopt a unified framework. Building on this prior work, the present study seeks to examine epistemological beliefs among both teachers and students within a shared analytical framework. By exploring role-specific patterns in beliefs about knowledge and learning, the study addresses gaps in existing Indian research, which typically considers either students or teachers in isolation. The findings are intended to inform both instructional practices and teacher education initiatives in the physical sciences, providing empirical evidence to guide future curriculum design and classroom interventions. This paper addresses this gap by presenting a study conducted using the EBAPS among distinct groups of science teachers in India. While prior research has examined epistemological beliefs of teachers in general, comparatively little attention has been paid to how these beliefs vary with demographic and professional factors such as gender and teaching experience, particularly within the Indian physical sciences context. Understanding these variations is important, as teachers' epistemological beliefs influence instructional practices, classroom discourse, and learning opportunities afforded to students. Accordingly, the present study explicitly examines teachers' epistemological beliefs with respect to gender and professional experience, alongside a comparison with students' beliefs. The remainder of the manuscript is organized as follows. Section 2 outlines the purpose of the study and the research objectives. Section 3 describes the methodology, Section 4 details the survey dimensions and the methodology used to assign weightage to individual question items. Section 5 presents the data analysis and results. Section 6 concludes the paper by summarizing the key findings, discussing implications, and finally Section 7 outlines directions for future research.

2 Purpose of Study

The purpose of the present study is to investigate epistemological beliefs concerning the nature of knowledge and learning in physical sciences among teachers across multiple educational levels (school, college, and university) and among undergraduate students. Using the Epistemological Beliefs Assessment for Physical Science (EBAPS), the study examines how participants conceptualize scientific knowledge, knowing, and learning, and evaluates the extent to which these beliefs correspond with expert perspectives in the discipline.

Research Questions The study is guided by the following research questions:

1. What epistemological beliefs about physical science and the learning of physical science are held by school teachers and faculty teaching at undergraduate and postgraduate levels in colleges and universities?

2. What epistemological beliefs about physical science and learning are held by undergraduate students?

3. To what extent do the epistemological beliefs of teachers and undergraduate students align with expert views of knowledge and learning in the physical sciences, as operationalized within the EBAPS framework?

3 Methodology

The present study employed a survey research design using the Epistemological Beliefs Assessment for Physical Science (EBAPS) to examine epistemological beliefs among teachers and students. The sample was drawn from selected school and higher education institutions in Shimla, Himachal Pradesh, India. The teacher sample comprised educators teaching at the Grade 12 level as well as faculty members teaching at the undergraduate (UG) and postgraduate (PG) levels. Grade 12 teachers were selected from three types of schools: a privately managed school, a centrally administered public school, and a state government run school. In addition, college and university faculty members teaching at the undergraduate and postgraduate levels were included. Details of the teacher sample are presented in Table I. The student sample consisted of third year undergraduate students from a women's degree college and of a public co-educational college located in Shimla, Himachal Pradesh, India (see Table II for sample details)

Table I: Details of the Sample of Teachers

School/College	Class Taught	Male	Female	Total
Teachers from privately managed school	Grade 12	40	10	50
Teachers from centrally administered public school	Grade 12	38	9	47
Teachers from state run Govt. school	Grade 12	32	4	36
Teachers from colleges and universities	UG & PG	34	6	40

Table II: Details of the Sample of Students

College	Class/Year	Male	Female	Total
Women's degree college	B.Sc. III	–	53	53
Public co-educational college	B.Sc. III	23	10	33

4 Survey Dimensions and Methodology of Weightage For Each Question Item

The Epistemological Beliefs Assessment for Physical Science (EBAPS) is a 30-item instrument designed to assess students' epistemological beliefs in physical science. Items include agree/disagree statements, multiple-choice questions, and debate items rated on a five-point Likert scale (0–4). The survey measures five epistemological dimensions. Structure of Scientific Knowledge evaluates whether science is perceived as a coherent body of knowledge or as disconnected facts. Nature of Knowing and Learning examines beliefs about learning as passive reception versus active knowledge construction. Real-Life Applicability assesses the perceived relevance of science beyond academic settings. Evolving Knowledge addresses views of scientific knowledge as fixed or subject to change through evidence-based inquiry. Source of Ability to Learn explores whether scientific ability is considered innate or developable through effort. Table III presents the item distribution across the five dimensions. Following EBAPS scoring guidelines, item scores (0=least sophisticated; 4=most sophisticated) were aggregated by dimension and multiplied by 25 to rescale each axis to a common 0–100 metric. This standardization ensures comparability across dimensions with unequal item counts and enhances interpretability without altering the relative weighting of items. The overall EBAPS score was calculated as the mean of the five axis scores to yield a composite measure of epistemological sophistication consistent with the instrument's theoretical framework. Learners' epistemological beliefs are commonly categorized as naïve or sophisticated [28]. Naïve beliefs reflect views of knowledge as certain, authority-based, and independent of effort, with ability perceived as fixed. Sophisticated beliefs emphasize the evolving, constructed nature of knowledge and the role of effort in learning. Consistent with prior studies, mean scores below 3 indicate naïve beliefs, while scores above 3 represent expert-like epistemological perspectives [29]. These criteria were adopted in the present study.

5 Data Analysis and Results

In the following section, we present the analysis of the gathered data and look at it in different ways: (5.1) Axis-wise, (5.2) Overall, (5.3) Experience-wise, and finally (5.4) Gender wise. As explained earlier, the EBAPS survey, a benchmark score of 3 represents the threshold between naïve and sophisticated epistemological beliefs. Because individual items are scored on a 0–4 scale, a mean score of 3 indicates consistent endorsement of expert-like responses across items within a given dimension. Scores below 3 reflect predominantly naïve or transitional beliefs, characterized by views of knowledge as fixed, authority-driven, and weakly connected to effort or

Table III: Dimensions of Five Axes in EBAPS

Axis	Axis Title	Dimension of Axis	Question items pertaining to each axis
Axis1	Structure of Scientific Knowledge *(coherent vs. pieces)*	Whether science is perceived as a coherent, unified body of knowledge or as a grouping of disconnected facts and formulae?	(2, 8, 10, 15, 17, 19, 20, 23, 24, 28)
Axis2	Nature of Knowing and Learning *(propagating from authority vs. self-constructed)*	Does learning science mean absorbing facts or constructing knowledge from prior knowledge, working with materials, and reflecting?	(1, 7, 11, 12, 13, 18, 26, 30)
Axis3	Real-Life Applicability *(applicable vs. non-applicable to real life)*	Can science apply only to a classroom or laboratory, or does it apply more generally to real life?	(3, 14, 19, 27)
Axis4	Evolving Knowledge *(absolute vs. changing)*	Is knowledge absolute, evolving as often as people's beliefs, or changing in a structured, research-based manner?	(6, 28, 29)
Axis5	Source of Ability to Learn *(inherent vs. acquired)*	Does being good at science result from natural ability, or can most people become better at learning and doing science?	(5, 9, 16, 22, 25)

real-world contexts. In contrast, scores at or above 3 signify sophisticated epistemological perspectives, including recognition of the evolving nature of scientific knowledge, active knowledge construction, and the role of effort in learning. Accordingly, the benchmark of 3 is used in this study to distinguish non-expert from expert-like epistemological orientations, consistent with prior EBAPS-based research.

5.1 Axis-wise Analysis

Axis 1 Structure of Scientific Knowledge This dimension probes whether individuals view science as a unified, cohesive entity or as a mere collection of disjointed facts and formulas. The average score across all

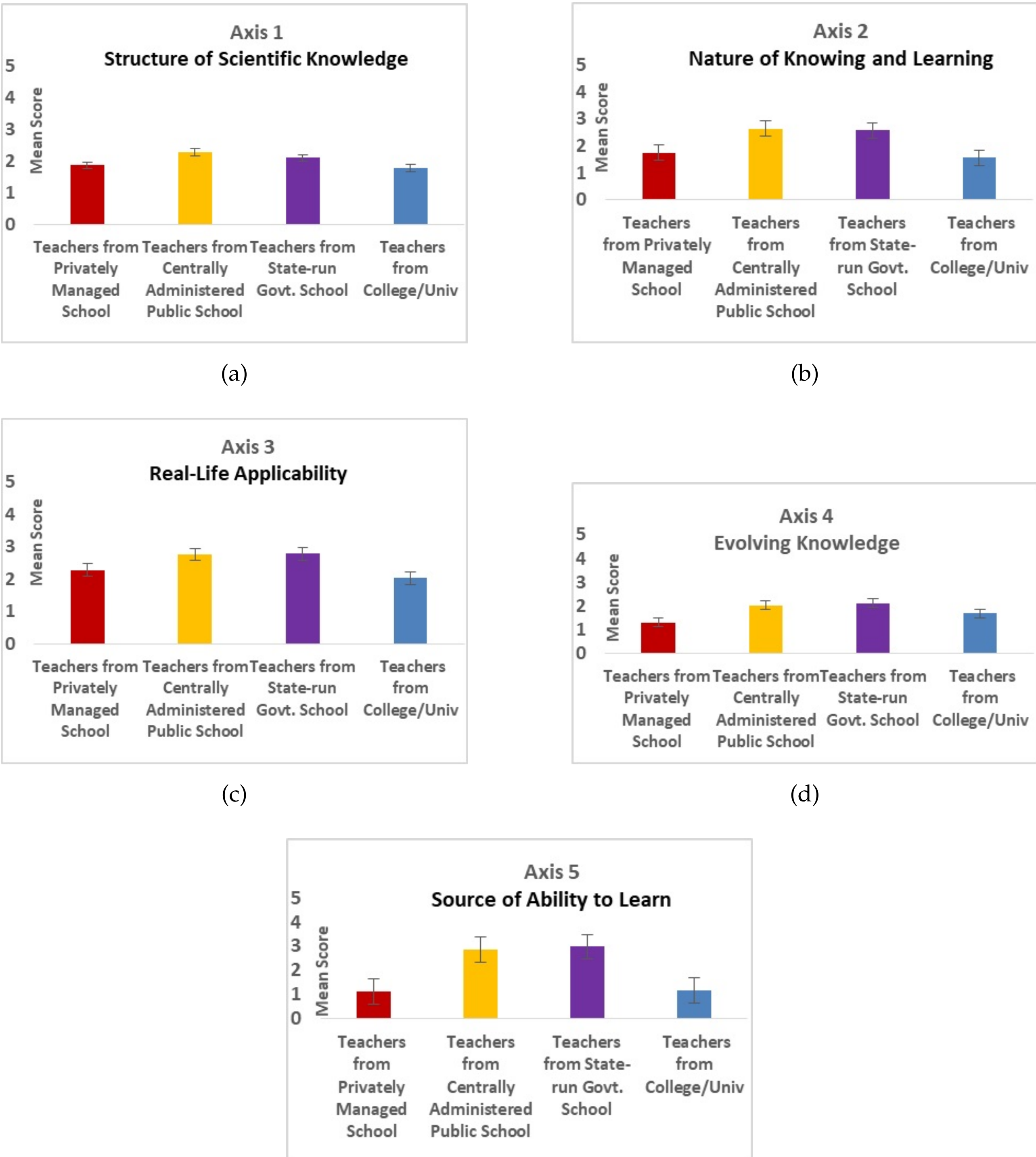

(a) (b) (c) (d) (e)

Figure 1: Axes-wise results of EBAPS for **teacher** samples.

fourteacher groups depicted in Figure 1a was found to be below 3, indicating a preva-

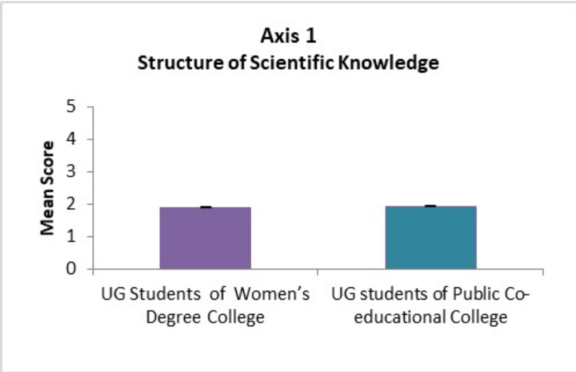

(a)

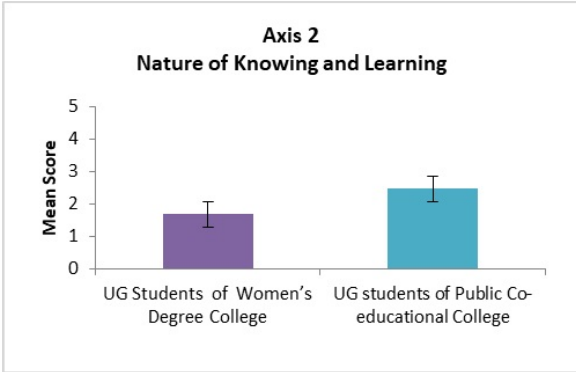

(b)

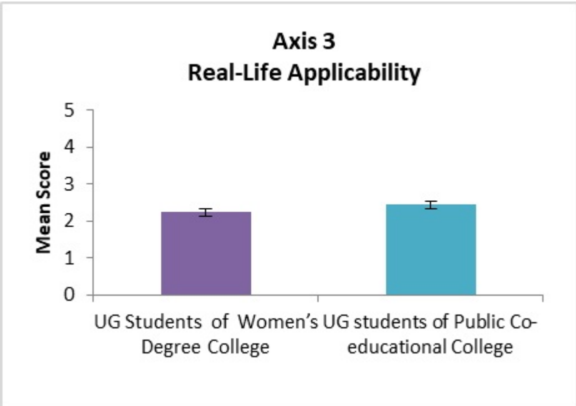

(c)

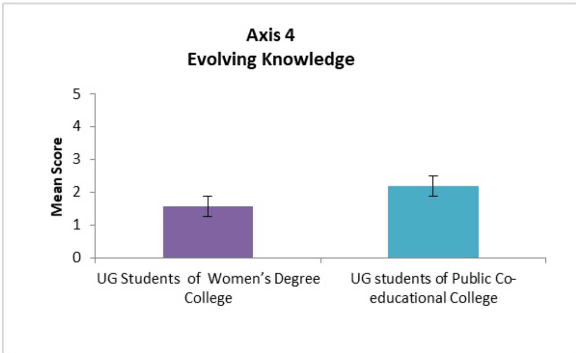

(d)

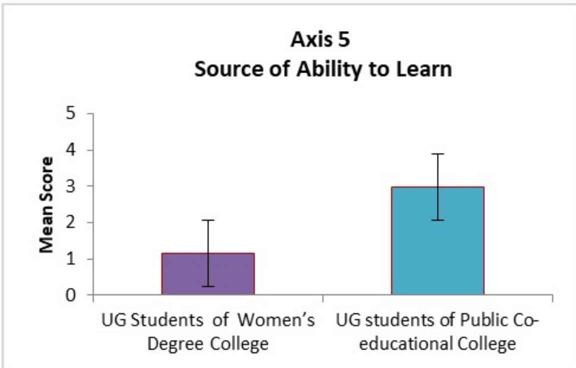

(e)

Figure 2: Axes wise result of EBAPS for **students** samples

lent tendency among teachers to perceive scientific knowledge in fragmented terms. Similarly, when examining undergraduate students, as illustrated in Figure 2a, those from both public co-educational college and from a women's degree college scored below 3. This suggests neither cohort exhibited an expert-like or sophisticated perspective regarding the coherence and structure of knowledge. Rather, both teachers and students tended to view knowledge as comprising discrete elements, characterized primarily by the memorization of facts, formulas, and isolated pieces of information.

Axis 2 Nature of Knowing and Learning In axis 2, the question arises: is learning science merely about passive absorption of facts, or is it about actively constructing knowledge through the integration of prior knowledge, hands-on engagement with materials, and reflective practice? The findings from both groups of teachers and students, as depicted in Figures 1b and 2b, respectively, indicate a mean score below 3. This suggests that a significant portion of both teachers and students perceive learning science as primarily centered around the passive absorption of information, rather than an active process of constructing personal understanding.

Axis 3 Real-Life Applicability Axis 3 examined beliefs related to the reallife applicability of science, specifically whether science is perceived as limited to classroom or laboratory settings or as extending to everyday contexts. The mean score obtained for this axis (Fig. 1c), across four groups of teachers, showed a slight improvement compared to the other axes; however, it remained below the expert-like benchmark of 3. Teachers from state-run government schools and centrally administered public schools scored nearly at the expert-like level, whereas teachers from privately managed schools and college-level institutions scored substantially lower. Similarly, the mean score for undergraduate students on this axis (Fig. 2c) also remained below 3.

Axis 4 Evolving Knowledge In axis 4, which explores whether knowledge is absolute or constantly evolving based on people's beliefs or structured research, the mean score among all groups of teachers was notably low (see Fig. 1d). Similarly, in the case of students (see Fig. 2d), the mean score for both colleges was below 3. These results suggest that both teachers and students found it challenging to grasp the concept that science is a dynamic process continually enriched by advancements in knowledge and learning.

Axis 5 Source of Ability to learn Axis 5 addressed beliefs concerning the origin of scientific proficiency, specifically whether competence in science is viewed as an innate ability or as a skill that can be developed through effort and exposure. The mean scores of teachers from state-run government school and centrally administered public school were close to the expert-like level (Fig. 1e), reflecting a belief that most individuals can improve their scientific learning and skills through effective study strategies. Such beliefs may positively influence students by fostering motivation to engage with scientific disciplines. In contrast, the mean scores of UG/PG level teachers and teachers from privately managed school were considerably lower, suggesting a tendency to view scientific aptitude as largely innate and less amenable to development over time. Students' responses on this axis are presented in Fig. 2e. Undergraduate students from public co-educational college demonstrated beliefs closer to the expert-like perspective, whereas students from the women's degree college scored substantially lower. Indicating different perceptions about whether the ability to learn science can be developed. Table IV and Table V present the descriptive statistics (Mean ± Standard Deviation) and one-way ANOVA results for the five axes across all the teachers' groups and students' groups. From the Mean ± SD table it is observed that Axis 3 consistently exhibited higher mean values across all groups, suggesting it represents a strongly developed or widely agreed upon dimension. In contrast, Axis 5 showed substantial variability, with notably higher scores in centrally administered and government school teachers as well as co-educational college students, but lower scores among private school, teachers from colleges and universities and students from women's degree college. This might be possible system-level or training-related differences or variation in exposure, resources, or pedagogical practices.

Table IV: Descriptive Statistics (Mean $\pm$ SD) for Teachers and Students Groups (rounded to two decimal places)

	Teachers from Privately Managed School	Teachers from Centrally Administered Public School	Teachers from state run Govt. Schools	Teachers from Colleges and Universities	Students from Women's Degree College	Students from Public Co-educational College
Axis 1	1.87 ± 0.60	2.29 ± 0.53	2.11 ± 0.45	1.76 ± 0.48	1.90 ± 0.49	1.93 ± 0.32
Axis 2	1.75 ± 0.45	2.67 ± 0.39	2.58 ± 0.50	1.56 ± 0.55	1.66 ± 0.62	2.46 ± 0.46
Axis 3	2.29 ± 0.85	2.86 ± 0.74	2.78 ± 0.70	2.04 ± 0.79	2.30 ± 0.83	2.47 ± 0.73
Axis 4	1.32 ± 0.67	2.04 ± 0.93	2.13 ± 0.75	1.73 ± 0.93	1.55 ± 0.83	2.14 ± 0.66
Axis 5	1.13 ± 0.47	2.86 ± 0.77	2.98 ± 0.60	1.16 ± 0.47	1.15 ± 0.60	3.00 ± 0.63

The analysis of mean scores across five axes revealed a consistent pattern of variation across the axes, irrespective of institutional context. A one-way ANOVA indicated statistically significant differences among the axes in every dataset (p ¡ 0.001), confirming that the observed variations are not due to chance. Furthermore, the magnitude of differences, as reflected by F-values ranging from 8.54 to 27.21, indicates considerable variability across axes, particularly among private school teachers. These findings highlight both common trends and institutional differences in the measured constructs.

Table V: One-way ANOVA Summary for Teachers and Students Groups

Dataset	F-value	p-value	Significance
Teachers from Privately Managed School	27.21	1.07×10^{-18}	Significant
Teachers from Centrally Administered Public School	9.72	2.1×10^{-7}	Significant
Teachers from state run Govt. Schools	13.25	1.57×10^{-9}	Significant
Teachers from Colleges and Universities	8.54	2.1×10^{-6}	Significant
Students from Women's Degree College	9.30	2.8×10^{-7}	Significant
Students from Public Co-educational College	13.67	3.2×10^{-9}	Significant

5.2 Overall Analysis

Figures 3a and 3b indicate that:

- The overall mean score across all four groups of teachers was below 3, indicating that none of the groups approached expert-like or highly sophisticated views.
- Among the teacher groups, those from centrally administered public schools and state-run government schools obtained the highest mean scores across all axes as well as overall; however, these scores still did not reach the expert-level benchmark..
- Teachers from privately managed schools and from colleges/universities exhibited consistently similar mean scores across all axes and overall, and these scores were markedly lower than expert-like levels.
- For undergraduate students from both public co-educational college and from a women's degree college, the mean scores across all axes remained below 3.

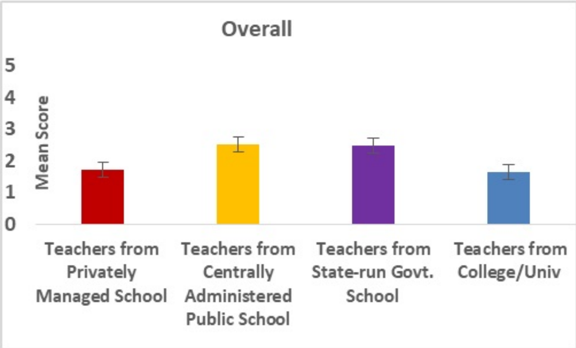

(a)

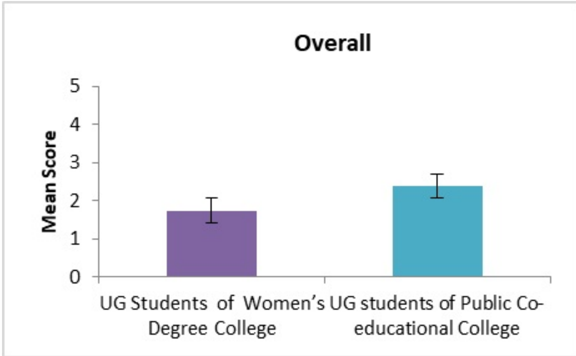

(b)

Figure 3: Overall result of teachers and students in EBAPS

5.3 Teaching Experience vs. Beliefs Analysis

Figure 4 gives the mean score of teachers holding different levels of teaching experience and showing a clear impact of teaching experience in acquiring expert-like views.

- The mean score of the teachers with an experience of more than 30 years was highest in almost all the axes, as well as overall.
- In axes 2, 3, and 5, teachers with vast years of experience, i.e., (36-40), had a mean score near 3, showing their expertlike beliefs.
- In axes 1 and 4, the mean score of all the groups was very low, irrespective of the years of experience

The result obtained above indicates that focused interventions are needed at the beginning of a teacher's career to sensitize them to the nature of science and the epistemology of scientific knowledge. While accurate content delivery is important, fostering scientific thinking and promoting inquiry-based learning in the classroom are equally critical. If left unaddressed, misconceptions or naïve epistemological beliefs may negatively influence instructional practices. Therefore, early and deliberate support in this area is vital to ensure that teachers develop a well-informed and reflective approach to science education.

5.4 Gender wise Analysis

The gender comparisons of teachers' and students' epistemological beliefs are presented in Figures 5(a) and 5(b). By identifying systematic gender differences, the study highlights underlying belief patterns that may subtly shape classroom dynamics and learning outcomes. The findings reveal that female teachers scored lower than their male counterparts in Axes 1, 2, 4, and 5. This suggests that female teachers tended to

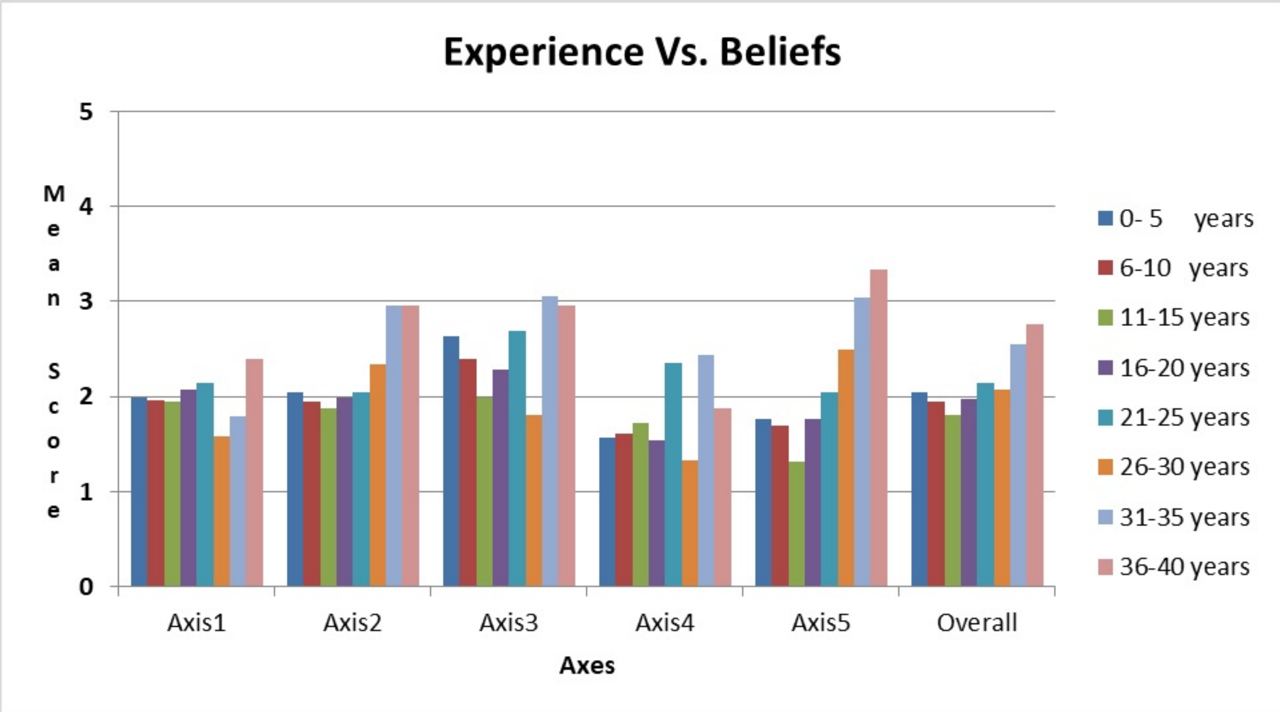

(a)

Figure 4: Experience vs. Beliefs result

lean more towards the belief that a person's ability is innate or fixed compared to male teachers. It raises important questions about how beliefs develop within professional and sociocultural contexts. This challenges common assumptions and suggests that epistemological beliefs are not merely individual traits but are influenced by broader structural, cultural, and institutional factors. Understanding these patterns is essential for designing targeted professional development that addresses belief systems, not just teaching techniques. Conversely, male teachers scored lower than female teachers in Axis 3, indicating a tendency towards naïve beliefs when relating subjects to real-life experiences. Identifying gender-linked tendencies in this dimension allows teacher educators and curriculum designers to intervene more precisely, strengthening contextual teaching approaches where needed. Among undergraduate students, females scored lower than males in all axes except Axis 1. It suggests potential differences in how male and female students conceptualize knowledge and learning during formative academic years. Gendered patterns appearing at both levels suggest that epistemological beliefs may be socially reinforced over time, rather than emerging in isolation. This underscores the need for early and sustained educational interventions that promote sophisticated, flexible, and growth-oriented epistemological beliefs across genders.

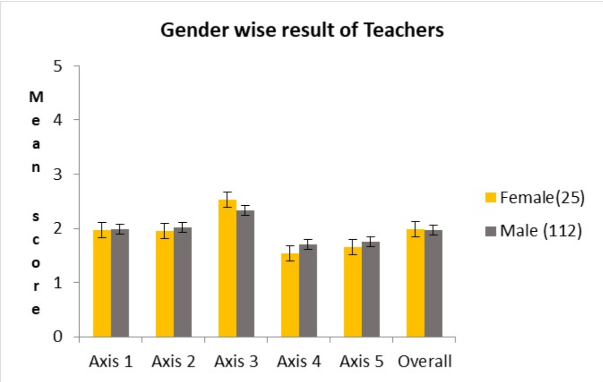

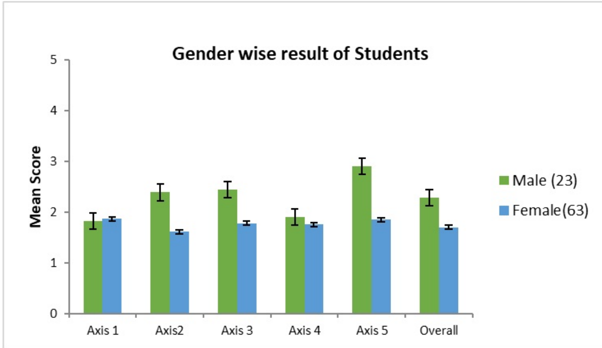

Fig. 5. Gender-wise comparisons of teachers' and students' epistemological beliefs.
(a) Teachers (b) Students

6 Conclusions

Epistemological beliefs offer important insights into both teaching and learning processes, because of that they have drawn a lot of attention in the academic literature within the education community. While students' beliefs influence how they approach learning tasks, interpret scientific knowledge, and participate in scientific inquiry, teachers' beliefs have an impact on instructional practices. Therefore, comprehending both viewpoints is crucial to enhancing science instruction. Using the Epistemological Beliefs Assessment for Physical Science (EBAPS) survey, which focuses on beliefs about the nature, acquisition, and comprehension of scientific knowledge, this study investigated the epistemological beliefs of teachers and undergraduate science students. Preliminary analysis indicated that both teachers and students predominantly perceived scientific knowledge as the memorization of facts, formulas, and discrete pieces of information. Additionally, participants in both groups found it difficult to understand how scientific knowledge is applicable and relevant in daily life. However, both teachers and students thought that improved study techniques and consistent effort may lead to success in learning science. Despite this belief in effort, neither teachers nor students exhibited the epistemological perspectives that are indicative of sophisticated or expert-like scientific understanding. These ideas may cause students to use superficial learning techniques, interact with concepts less, and have trouble applying what they've learned to new or real-world situations. These ideas may limit teachers' ability to educate, favoring fact-based methods over inquiry-based or conceptual learning opportunities. Thus, epistemological assumptions are crucial in determining how education is shaped as well as how students learn, how motivated they are, and how they view scientific literacy. The results highlight the necessity of prompt and deliberate interventions aimed at both educators and learners. While instructional strategies and curriculum designs at the undergraduate level should specifically support students' understanding of science as a dynamic, interconnected, and meaningful enterprise, professional development initiatives should assist teachers in developing more sophisticated epistemological perspectives. Efforts to improve the quality of science education and learning results are likely to remain limited if epistemological views on both sides of the classroom are not addressed.

7 Future Directions

This study provides an opportunity to learn about physical science teachers' and students' epistemological beliefs, but the fact that it includes responses from participants from only few institutions makes generalizations difficult. Further studies might apply larger institutionally connected samples, mixed-method approaches, or longitudinal designs to explore how epistemological beliefs develop and relate to teaching. This type of work can also help to inform teacher education, curriculum development and classroom interventions aimed at promoting more sophisticated epistemic orientations in science education.

8 Acknowledgements

The authors sincerely thank the Editor and the anonymous reviewers for their careful evaluation of the manuscript and for their constructive and insightful comments.

References

[1] C. Wieman and K. Perkins (2005). Transforming Physics Education. *Physics Today*, 58(11), 36–37.

[2] M. Schommer (1993). Epistemological development and academic performance among secondary students. *Journal of Educational Psychology*, 85(1), 406–411.

[3] C. M. Czerniak, A. T. Lumpe, and J. J. Haney (1999). Science teachers' beliefs and intentions to implement thematic units. *Journal of Science Teacher Education*, 10(2), 123–145.

[4] B. Laplante (1997). Teachers' beliefs and instructional strategies in science: Pushing analysis further. *Science Education*, 81(3), 277–294.

[5] S. Sharma and P. K. Ahluwalia (2012). Diagnosing Alternative Conceptions of Fermi Energy among Undergraduate

Students. *European Journal of Physics*, 33, 883.

[6] S. Sharma, P. K. Ahluwalia, and S. K. Sharma (2013). Students' Epistemological Beliefs, Expectations and Learning Physics: An International Comparison. *Physical Review Special Topics–Physics Education Research*, 9, 010117.

[7] I. Halloun and D. Hestenes (1985). The Initial Knowledge State of College Physics Students. *American Journal of Physics*, 53, 1043–1055.

[8] A. Elby (2011). Getting Started with Research on Epistemologies and Expectations. *Reviews in PER*, Vol. 2: *Getting Started in PER*, edited by C. Henderson and K. A. Harper. American Association of Physics Teachers. http://www.percentral.org/items/detail.cfm?ID=8805.

[9] V. Richardson (1996). The Role of Attitudes and Beliefs in Learning to Teach. In J. Sikula (Ed.), *Handbook of Research on Teacher Education*, pp. 102–119. New York: McMillan.

[10] F. M. Pajares (1992). Teachers' Beliefs and Educational Research: Cleaning Up a Messy Construct. *Review of Educational Research*, 62(3), 307–322.

[11] J. D. Miller (1989). Scientific Literacy. Paper presented at the Annual Meeting of the American Association for the Advancement of Science, San Francisco, California, 23p.

[12] J. D. Miller (1998). The Measurement of Civic Scientific Literacy. *Public Understanding of Science*, 7, 203.

[13] A. A. E. Panergayo (2023). Self-efficacy, Epistemological Beliefs, and Academic Performance in Physics: A Mediation Analysis. *Philippine Social Science Journal*, 6(2), 46–52.

[14] A. A. E. Panergayo, C. F. Gregana, J. F. D. Panoy, and E. N. Chua (2023). Epistemological Beliefs and Academic Performance in Physics of Grade 12 Filipino STEM Learners. *Jurnal Pendidikan Progresif*, 13(1), 16–24.

[15] E. Bahcivan, N. Yavuzalp, and M. Kilic (2024). Investigating Structural Relations among University Students' Self-efficacy Beliefs, Epistemological Beliefs, and Digital Literacy Skills. *World Journal on Educational Technology: Current Issues*, 16(3), 146–163.

[16] M. M. Alpaslan (2023). Investigating Girl and Boy High School Students' Epistemological Beliefs in Biology and Physics. *Online Science Education Journal*, 8(2).

[17] Johnson and Willoughby (2018). Epistemic Belief Structures within Introductory Astronomy. *Physical Review Physics Education Research*, 14, 010135.

[18] Chen (2019). Variations in Students' Epistemological Beliefs towards Physics. *Physical Review Physics Education Research*, 15, 010106.

[19] E. F. Redish, J. M. Saul, and R. N. Steinberg (1998). Student Expectations in Introductory Physics. *American Journal of Physics*, 66, 212.

[20] I. Halloun and D. Hestenes (1998). Interpreting VASS Dimensions and Profiles for Physics Students. *Science Education*, 7, 553.

[21] W. K. Adams, K. K. Perkins, N. Podolefsky, N. D. Finkelstein, and C. E. Wieman (2006). A New Instrument for Measuring Student Beliefs about Physics and Learning Physics: The Colorado Learning Attitudes about Science Survey. *Physical Review Special Topics–Physics Education Research*, 2, 010101.

[22] A. Elby, J. Frederiksen, C. Schwarz *et al.* Epistemological Beliefs Assessment for Physical Sciences (EBAPS). http://www2.physics.umd.edu/~elby/EBAPS/home.htm.

[23] B. K. Hofer and P. R. Pintrich (1997). The Development of Epistemological Theories: Beliefs about Knowledge and Knowing and Their Relation to Learning. *Review of Educational Research*, 67(1), 88–140. DOI: https://doi.org/10.3102/00346543067001088.

[24] D. Hammer and A. Elby (2002). On the Form of a Personal Epistemology. In B. K. Hofer and P. R. Pintrich (Eds.), *Personal Epistemology: The Psychology of Beliefs about Knowledge and Knowing*, pp. 169–190.

[25] S. Sharma, P. K. Ahluwalia, and S. K. Sharma (2013). Students' Epistemological Beliefs, Expectations, and Learning Physics: An International Comparison. *Physical Review Special Topics–Physics Education Research*, 9(1), 010117. DOI: https://doi.org/10.1103/PhysRevSTPER.9.010117.

[26] A. Sen and A. Karwande (2025). Exploring Epistemological Beliefs of Higher Education Teachers: Influences of Demographic and Professional Variables. *IOSR Journal of Research & Method in Education (IOSR-JRME)*, 15(3), 50–55. Retrieved from https://www.iosrjournals.org/iosr-jrme/papers/Vol-15%20Issue-3/Ser-3/F1503035055.pdf.

[27] Homi Bhabha Centre for Science Education. Episteme Conference. https://www.hbcse.tifr.res.in/academic/episteme-conference.

[28] M. Schommer (1994). Synthesizing Epistemological Beliefs Research: Tentative Understandings and Provocative Confusions. *Educational Psychology Review*, 6, 293–319.

[29] F. Örnek (2015). Pre-Service Science Teachers' Epistemologies in the Physical Sciences. *Bayburt University Journal of Education Faculty*, 10(1), 1–6.

Number of Trials Needed for an Experiment: A Statistical Approach

Poovizhi M[1] and V. Madhurima[1]

[1]Department of Physics, Central University of Tamil Nadu, Thiruvarur, India.
poovizhimaruthi@gmail.com; madhurima@cutn.ac.in

Submitted on 06-05-2026
Accepted on 02-06-2026

Abstract

Repeated measurements are fundamental to scientific methodology. However, many are unaware of the number of trials required for any given experiment. We ask and answer an important question - "are the required number of trials fixed for all the experiments?". We present a simple statistical framework taking the examples of length measurement using a vernier callipers and of percolation of water.

1 Introduction

Repeatability and reproducibility, i.e., obtaining the same results when the experiments are conducted under the same conditions, either by the same person or someone else, are crucial for scientific rigour. The natural question that follows is "how many times?". Students often have similar responses, and explanations, to the question of how many times they should repeat the measurement of length using vernier callipers. It is fairly common to hear 2 (check both values are same), 3 (three points make a straight line), 5 (teacher told us) or 6 (just feel like it). When the question extends to any other experiment, the common responses are the same as with Vernier Callipers, or that they do not have an idea!.

The answer to this question is not intuitive, it is deeply seated in statistics. When an experiment is performed we usually repeat the experiment before presenting the result. But have we asked "why do we repeat that?" or "how many times do we repeat it and is the repetition same for all the experiments". The answer to these questions can be found from the "law of large numbers" in statistics, which states that as the number of observations increases, the sample mean gets closer to the true population mean. In other words, with a large enough number of measurements, the average is a reliable estimate of the true value.

The number of observations required

depends on the variability of the data. If the variance is small, the sample mean stabilizes quickly and fewer observations are needed. If the variance is large, more observations are required for the sample mean to closely approximate the true mean. This idea governs the number of trials required. Let us explore this a little further.

2 Statistical Description of Measurements

When a physical quantity is measured repeatedly in an experiment, we usually do not obtain exactly the same value each time. Therefore, instead of relying on a single measurement, we perform the experiment multiple times and analyze the set of observations statistically.

For a set of (n) measurements (x_i), the arithmetic mean is defined as the sum of all data divided by the number of data and is given by

$$\bar{x} = \frac{1}{n}\sum_{i=1}^{n} x_i. \tag{1}$$

The mean represents the best estimate of the true value based on the available measurements, as shown in Figure 1.

The standard deviation, which shows the spread of data around the mean, is given by

$$\sigma = \sqrt{\frac{1}{n-1}\sum_{i=1}^{n}(x_i - \bar{x})^2}. \tag{2}$$

It quantifies how much the individual measurements fluctuate about the mean and therefore reflects the consistency (precision) of the experiment,

To compare variability across different experiments, especially when the measured quantities or their magnitudes are different, the coefficient of variation is defined as

$$CV = \frac{\sigma}{\bar{x}}. \tag{3}$$

Since it expresses the spread relative to the mean, it allows meaningful comparison of precision between experiments with different scales or units. For example, in the vernier calliper measurements, the same standard deviation (e.g., 0.1 mm) represents a much larger relative uncertainty for a 10 mm object than for a 100 mm object. The coefficient of variation accounts for this by expressing the spread relative to the mean, allowing meaningful comparison of precision across measurements of different magnitudes.

The standard error is defined as the uncertainty associated with the mean and is given by

$$SE = \frac{\sigma}{\sqrt{n}}. \tag{4}$$

It indicates how precisely the mean has been determined and decreases as the number of measurements increases.

For measurements with small fluctuations, repeated readings tend to cluster around a central value and may be approximated by a normal distribution.

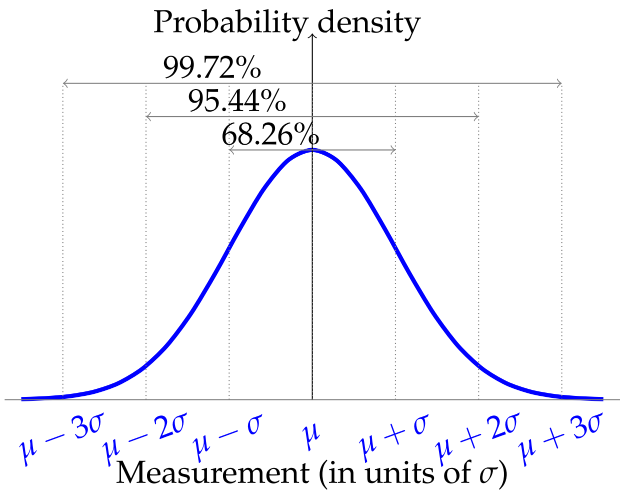

Figure 1: Normal distribution curve

3 Estimation of Required Number of Trials

Let us consider the case where we have obtained a large dataset. Many natural and experimental measurements approximately fit a normal distribution, which is a symmetric, bell-shaped distribution in which most measurements cluster around the mean and fewer occur as we move away from it.

For repeated measurements of a length using a vernier caliper, if the readings follow a normal distribution, the 95% confidence interval for the true length is

$$[\bar{x} \pm z \cdot SE]$$

Here, $(\bar{x})$is the average of the vernier readings and (SE) reflects how precisely that average has been determined from repeated measurements. The $(z) - value$ (1.96 for 95% confidence interval) comes from the normal distribution and represents how many standard deviations around the mean capture most of the repeated vernier measurements.

For such data, a 95% confidence interval for the mean is given by

$$\bar{x} \pm z \cdot SE. \tag{5}$$

where the z-score comes from the normal distribution table and is given by how many $x\,\sigma$ a data point is away from the mean.

Z-score	Left tail %	Confidence level
1.00	84.1%	68%
1.96	**97.5%**	**95%**
2.00	97.7%	95.4%
3.00	99.9%	99.7%

Table 1: Z value and the confidence level

For a 95% confidence interval,

$$\bar{x} \pm 1.96 \cdot SE \qquad SE = \frac{s}{\sqrt{n}},$$

[1, 2]

if a relative precision E is required (i.e., the half-width of the interval is at most $E\bar{x}$), then

$$1.96\frac{s}{\sqrt{n}} \leq E\bar{x}.$$

Using $CV = \frac{s}{\bar{x}}$, this gives

$$n \geq \left(\frac{1.96 \times CV}{E}\right)^2.$$

Thus, the required number of trials increases with the square of the coefficient of variation: experiments with larger relative spread require more repetitions to achieve the same precision.

Usually, one of the first laboratory experiments is the vernier caliper measurement, where students are often asked to take six readings. One may ask: why six, and not three, five, or ten? The above statistical result provides the justification.

Suppose six measurements of a metal block thickness give a mean of 5.218 mm and a standard deviation of 0.327 mm, corresponding to a coefficient of variation of 6.27%. For a required relative precision of $E = 5\%$, the required number of trials is

$$N = \left(\frac{1.96 \times 0.0627}{0.05}\right)^2 = (2.456)^2 \approx 6.$$

Thus, for this level of variability, six vernier readings are statistically justified.

4 Is this universally constant?

The value $N \approx 6$ is not universal. The required number of trials depends on the variability of the system being studied.

To illustrate this, consider a percolation simulation (for example, water flowing through a porous medium). In percolation, flow occurs only if a continuous path spans the system. Because the placement of blocking particles is random, even a single blockage can completely stop the flow. This makes the outcome highly variable from trial to trial.

To study this variability quantitatively, we use a computational model of percolation implemented in NetLogo. NetLogo is an agent-based modelling platform in which individual elements of a system (such as open or blocked sites) are treated as independent agents that follow simple rules. We use the site-percolation model where each lattice site is randomly assigned as open or blocked with a given probability, and percolation occurs only if a connected cluster of open sites spans from one side of the system to the other. The global behavior of the system then emerges from these local interactions. By running the simulation many times under identical conditions, we can measure how much the outcome fluctuates from trial to trial.

A stochastic percolation simulation is performed in NetLogo, three particle sizes mimicking sandy clay is implemented in the percolation simulation. This produced a mean wet percentage of approximately 34% with a standard deviation of 10.29%, giving a coefficient of variation of 30.3%. This is much larger than in the vernier experiment (where $CV \approx 6.27\%$), indicating that the percolation outcomes fluctuate far more strongly from trial to trial. In other words, the system is intrinsically more variable.

Using the same relative precision $E = 5\%$, we obtain

$$N = \left(\frac{1.96 \times 0.303}{0.05}\right)^2 = (11.88)^2 \approx 141 \text{ trials}.$$

Experiment	CV	N ($E = 5\%$)
Wire (student)	6.25%	**6**
NetLogo Wet%	30.3%	**141**

Table 2: Trials needed for standard 5% lab precision

Thus, for the same lab precision of $E = 0.05$ percolation requires many more trials because the system has much larger inherent variability. N $\propto$ (CV)^2 explains the dramatic difference.

5 Conclusion

The required number of trials in an experiment is not a fixed or universal number. It depends on the intrinsic variability of the system being studied. Experiments with small relative fluctuations such as vernier calliper measurements require only a few repetitions to achieve a given precision. In contrast, highly stochastic systems such as percolation exhibit large trial-to-trial variability and therefore require many more repetitions to estimate the mean with the same confidence and precision.

In general, for a desired relative precision E at 95% confidence, the required number of trials is given by

$$N = \left(\frac{1.96\,CV}{E}\right)^2.$$

This relation shows that the number of trials scales with the square of the coefficient of variation and increases rapidly for highly variable systems.

References

[1] P.R. Bevington and D.K. Robinson, *Data Reduction and Error Analysis for the Physical Sciences*, 3rd ed., McGraw-Hill, 2003.

[2] J.R. Taylor, *An Introduction to Error Analysis: The Study of Uncertainties in Physical Measurements*, 2nd ed., University Science Books, 1997.

[3] C.M. Prestwood and K.V. Hartley, *Statistical Methods in Experimental Physics*, North-Holland, 1970.

[4] U. Wilensky, "NetLogo Percolation model," *Center for Connected Learning, Northwestern University, 1997*.

Practical Teaching Note on Systematic Approach to Record and Reconstruct Hologram at Undergraduate level

Govind Kushwaha[1], Vishal Gupta[1], Ankush Rana[1], Sanjay Kumar[2] and Amit Garg[1*]

[1]Department of Electronics,
Acharya Narendra Dev College, University of Delhi,
New Delhi, India
*E-mail: amitgarg@andc.du.ac.in

[2]Department of Physics,
Acharya Narendra Dev College, University of Delhi,
New Delhi, India

(Submitted 30-10-2025)
(Accepted 13-04-2026)

Abstract

Ever since the invention of holography in 1948 (theoretically) and in 1962 (experimentally), it has continuously fascinated optics enthusiasts. There is so much learning in building into setting up a successful holography recording and reconstruction system. However, the failure to carry out successful recordings of a hologram is demotivational and acts as a big deterrent. We report here practical teaching notes on systematic approach to successfully record and reconstruct a hologram with locally available low-cost components. It is truly understood that holography is a well-established technique. However, in this paper we have attempted to present to the minutest details the intricacies involved in hologram recording and made an effort to address the possible failure points. The success of the approach has been ratified with scores of undergraduate students successfully carrying out recording and reconstruction of the hologram with 100% success rate. They have adopted 'Train the Trainer approach' and have trained their peers, leading to creation of a pool of successful hologram recording enthusiasts at UG level. It is envisaged that the present work will encourage optics enthusiasts and facilitate successful hologram recording and reconstruction.

1. Introduction

Holography is a captivating technique that elucidates through the principles of interference. The term "holographic" derives from the Greek words "holos," meaning "whole," and "graphe," signifying "drawing," encapsulating a technique that initially captured the complete light field information, encompassing both amplitude and phase [1]. Dennis Gabor, acknowledged as the progenitor of holography, was awarded the Nobel Prize in Physics in 1971 for his groundbreaking invention and development of the holographic method [2].

Holography serves as a fascinating experiment that ignites students' interest in the field of optics. Previous endeavors, such as those by E. A.Franke, and J. M. Franke, have focused on demonstrating and applying holography for undergraduate students [3]. Pombo et al. have underscored the utility of holography as a teaching tool, illustrating its efficacy in experimental optics teaching and its potential to inspire a profound interest in the study of physics at the school level [4].

Furthermore, advancements in technology have leveraged holography as an alternative to learning technology. Comparative studies have been conducted to evaluate the effectiveness of holographic teaching in Information and Communication Technology (ICT) [5-6]. This paper provides a comprehensive, step-by-step guide to ensure the successful recording and reconstruction of holograms. Notably, this approach is advantageous due to its simplicity, making it easily comprehensible for undergraduate students, and its implementation can be achieved using cost-effective components and equipment that are mostly available in any optics/photonics laboratory. The learnings from this experiment can be extended to set-up various type of interferometers for their multiple potential applications.

1.1 Basic Principle of Hologram

Holography, a groundbreaking imaging technique, captures and reconstructs three-dimensional images using the principles of light interference and diffraction. The process of studying holography involves two main steps: recording the hologram and reconstructing it using lasers or white light. Unlike traditional photography, in which we capture only intensity information, in holography, we record both the intensity and phase of scattered/reflected/diffracted light waves, resulting in lifelike, three-dimensional representations [7].

The fundamental holographic process involves splitting coherent laser light into two beams—an object beam and a reference beam. The object beam interacts with the subject to be imaged, and the resulting interference pattern is recorded on a photosensitive medium (here, we have used silver halide photographic emulsions). During playback, when illuminated by the reference beam, the recorded interference pattern reconstructs the original three-dimensional scene. This versatile technique finds applications in art, entertainment, scientific visualization, microscopy, interferometry, and security.

The elegant interplay of light's wave nature and interference in holography showcases the transformative ability of science to sculpt three-dimensional illusions before our eyes. Advancement in lasers, photosensitive film/plate, and methods of demonstration have all combined to allow holography to be studied in graduate, undergraduate, and school levels. The demonstration generate interest among all - science, engineering and art students. The positive attitude is not only from undergraduate students but also from school teachers and students. It is now well established that holography can be used as a teaching tool with great success and highly motivating for the experimental teaching. It has truly encouraged the students towards optics education at the undergraduate level.

For a deeper understanding of holography principles and applications, interested readers can refer to the roadmap on holography published by John T. Sheridan et al. in 2020 (J. Opt. 22, 123002) [8]. This comprehensive review explores holographic theory, advancements, and emerging trends, providing valuable insights for researchers, students, and enthusiasts. To further delve into the scientific intricacies of holography, resources such as "Basic Principles and Applications of Holography" and "Basic Principle of Holography - Engineering Physics" ([9,10]) can be consulted. In addition, one can refer the book [11] by Saxby for deep knowledge of Practical Holography. Further, in another work by Salancon etal. [12] they have upgraded some of the previous developments to make colour holograms. However, the use of a high power 20mW He-Ne laser makes the development cost ineffective. Though there is abundant literature available including some of the above listed important references, there are no crisp recipes described for a sure shot successful hologram recording.

The significance of this work lies in its potential to democratize access to holography, making it an accessible and feasible learning tool for educational institutions with limited resources. The step-by-step instructions offered in this paper serve as a valuable practical teaching note for individuals seeking a failure-free experience in both recording and reconstructing of holograms. By breaking down the process into detailed instructions highlighting the important steps that lead to the failure of the hologram recording, the paper empowers users with the knowledge to implement holography techniques successfully, fostering a sense of self-reliance and accomplishment at very low cost.

Thus, the present work suits the best for Indian University/colleges/school system if they want to demonstrate this wonderful optics learning through holography. The unique feature in this paper is that the complete experiment was set-up and conducted independently by undergraduate students with 100% success rate. This is the result of our belief as we highly emphasize on 'train the trainer' philosophy under the SPIE Student Chapter University of Delhi at Acharya Narendra Dev College. In the present paper, cost-effective methodology has been explained and authors emphasize to popularize holography in university, colleges and schools.

2. Experimental Setup

This section provides a comprehensive overview of the equipment employed in the holographic recording and reconstruction experiment. It is emphasized here that we have not discussed the detailed technical specifications of each of the components but described them in general. These components are available in routine from various scientific suppliers in India at affordable costs. Following a detailed component/equipment description, a clear and concise diagram of the experimental setup is presented. Towards the end, a step-by-step procedure guiding the readers through the recording and reconstruction processes is presented for easy and successful replication.

2.1 Components/Equipment Details

2.1.1Beam Splitter

It is used to split the incident light beam into two separate beams by a designated intensity ratio as shown in Fig.1. Additionally, beamsplitters can also be used in reverse to combine two different beams into a single one. Beamsplitters are classified according to their construction. We have used a single beam splitter 30/70 in the present experiment.

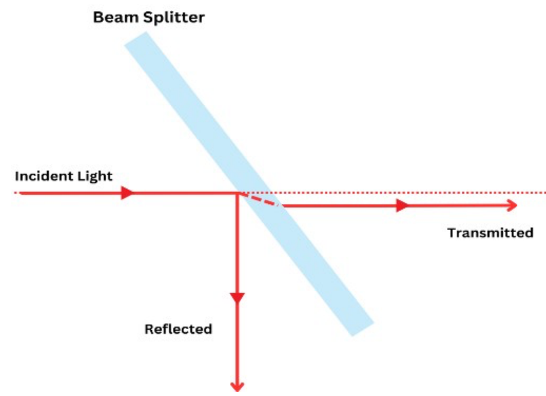

FIG. 1: Ray diagram of the Beam Splitter.

2.1.2 Optical Mirror

It is an optical component used to reflect the laser light in any direction. Since they are having 100% (approximately) reflectivity, the incident beam is mostly reflected in the desired direction. A mounted 2” diameter optical mirror is as shown in Fig.2. We have used two such optical mirrors in the present set-up.

FIG. 2: A mounted Optical Mirror of 2” diameter.

2.1.3 Microscope Objective (MO)

It consists of a multi lens system and is used to magnify the spot size of the input laser beam. The basic parameters that are usually specified for a MO are its magnification, numerical aperture; lens image distance and cover slip thickness specified in mm [13]. Fig. 3 shows the MO used in the present experiment having the following specification: magnification 10X, numerical aperture 0.25; lens image distance 160mm and cover slip thickness 0.17mm. We have used two such MOs in the present set-up. The magnification should be chosen such that the beams can cover the whole object and the reflected rays are projected on the photographic film.

FIG. 3: Mounted Microscope Objective.

2.1.4 Mechanical Mounts/ Supports

These are different types of mechanical hardware that holds optical components such as an object holder, microscope objectives holder, sandwiched photographic film holder etc. (Fig. 4 (a) - 4(c)). We can easily mount the bases of these optical mounts on an optical breadboard using M6 LN screws. They provide stability to the overall equipment set-up to ensure the minimum vibrational disturbance.

(a) *(b)* *(c)*

FIG. 4: (a) An object holder on which the object is mounted using a hot glue gun. (b) A Microscope Objective holder. (c) A photographic film holder.

2.1.5 Photographic Film

The recording medium employed is PFG-01[14], a red sensitive (for 632.8 nm), high resolution photographic film comprising of silver halide. These are specially designed for recording holograms using a continuous wave laser, a red He-Ne laser in the present case. They are to be processed in green light. We have used the standard Kodak D-76 developer and Sodium Thiosulphate as fixer. Fig. 5 shows a developed photographic film.

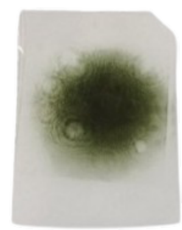

FIG. 5: Hologram (Developed Photographic Film).

2.1.6 Laser

We have used a 2mW He: Ne laser (Fig. 6) that emits a bright red laser beam whose wavelength is 632.8 nanometers.

FIG.6: A 2mW He: Ne Laser [15]

2.1.7 Object

In this case, we are taking an object (Fig. 7) made of marble whose 3D image will be recorded on a high-resolution photographic plate. One can choose any similar object for this purpose.

FIG. 7: Object in the form of marble Shivling.

2.1.8 Optical Breadboard

It is an optical tabletop (a part of vibration isolation system) that is used to mount systems used for laser and optics-related experiments in science, engineering, and manufacturing through an array of M6 threaded holes or magnetic bases. The surfaces of these tables are designed to be very rigid with minimum deflection so that the alignment of optical elements remains stable over time. Many optical systems require that the vibration of optical elements be kept to minimum. As a result, optical tables are typically very heavy and incorporate vibration isolation and damping features in their structure, reducing the ability of vibrations in the floor to cause vibrations in the tabletop. The surface of an optical table is typically ferromagnetic steel with a honeycomb structure inside and has a rectangular grid of tapped M6 holes in either metric or imperial units [16]. They can be placed on an ordinary table or workbench or on specially designed vibration isolation systems. A typical optical breadboard is as shown in Fig. 8. In the present experiment, we have used an already available optical breadboard in the lab of size 6' x 4'. A size of 2' x 3' is sufficient to carry out such type of hologram recording.

FIG. 8: An Optical Breadboard [17].

2.1.9 Tyre's Inner Air Tube

Since vibration isolation systems cost around USD 2500, we have used two-wheeler vehicle tyre's inner air tubes (Fig. 9) beneath the optic table top instead of vibration isolators. This makes our experimental setup more cost-effective and simpler for users by providing required vibration isolation to carry out holography recording successfully. We have used four such tubes placed at the four corners of the optical bread board. The pressure in the tube is adjusted to 20 psi for best results.

FIG. 9: Image of a Tyre's Inner Air Tube [18].

2.1.10 Glass Plates

In this experiment, we have used two glass plates (Fig. 10) of size 2" x 2" to sandwich the photographic film. This arrangement keeps the films straight as well as reduces the cost of expensive holographic plates.

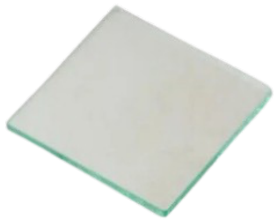

FIG. 10: A Glass Plate.

The component numbers and their tentative cost is as mentioned in the Table 1(a) with comparative cost break up as Table 1(b) below:

Table 1(a): Cost break-up

S. No.	Item Name	Quantity	Unit cost (Ex-Works) INR
1.	He: Ne Laser (2 mW)	01	45000
2.	Laser Holder Mount	01	3500
3.	Beam Splitter 2”	01	1850
4.	Beam Splitter Holder 2”	01	1600
5.	Mirror 2”	02	2000
6.	Mirror Holder 2”	02	1600
7.	Microscope Objective (MO)	02	2000
8.	MO Holder	02	1200
9.	Plate holder	02	2000
10.	Processing Trays	03	400
11.	Film	1 Set	9500
12.	Chemicals	01 Set	4000
13.	Safe (Green) light	01	900
14a.	Table Top (4 feet x 4 feet x 2.4” approx.)	01	1,25,000
14b.	Vibration Isolators	04	-
14c	Tyre’s Inner Tubes	04	400
15.	Air Pump (Foot Pump)	01	500
16.	Polarizing Sheet 2”x2”	01 (2”x2”)	300
17.	M6 Screws with Key	01 Set	800
18.	Miscellaneous Items	01 Set	4000

Table 1(b): Comparative Cost break-up

S.No. (corresponding to Table 1(a))	Unit cost (Ex-Works) INR (corresponding to Table 1(a))	Unit Cost (CIF) (USD)	Total Cost (CIF) of equipment / components of Our Set-Up (USD)*	Total Cost (CIF) of equipment / components in the optical research laboratory (USD)**
1.	45000	550	550	2300
2.	3500	40	40	130
3.	1850	22	22	50
4.	1600	20	20	55
5.	2000	25	50	280
6.	1600	20	40	110
7.	2000	25	50	2400
8.	1200	15	30	50
9.	2000	25	50	90
10.	400	05	15	15
11.	9500	128	128	128
12.	4000	50	50	50
13.	900	12	12	12
14a.	1,25,000	1600	1600	3200
14b.	-	-	-	2500
14c	400	5	20	-
15.	500	8	8	8
16.	300	5	5	105
17.	800	10	10	10
18.	4000	50	50	50
	Total cost (CIF)		**2750**	**11543**

* The latest price of all the equipments/components as taken from the Indian supplier(s).

** The price of most of the optical and mechanical equipments/components may be verified any time from the supplier. Some (Ex-works) prices from ThorLab (ThorLab.com). are given for the ready reference:

Microscope Objective : 9.458,50 €
Laser : 1.770,87 €
Laser mount : 113,79 €
Beam splitter 30/70 : 37,27 €
Mirror Holder : 42,75 €
Mirror 2” : 111,58 €
Microscope Objective holder : 18,57 €
Glass plate holder : 71,93 €
Polarizer Plane 2” diameter : 88,38 €
4 leg vibration isolators set : 1.973,85 €
Bread Board Table Top : 2.140,65 €

Any research optics lab will have most of these equipment/components. We have used here very cost effective equipments/components and successfully completed the process of recording and reconstruction of holograms in our undergraduate laboratory.

2.2 Setup Diagram and Methodology

2.2.1 Setup Diagram for Recording of Hologram

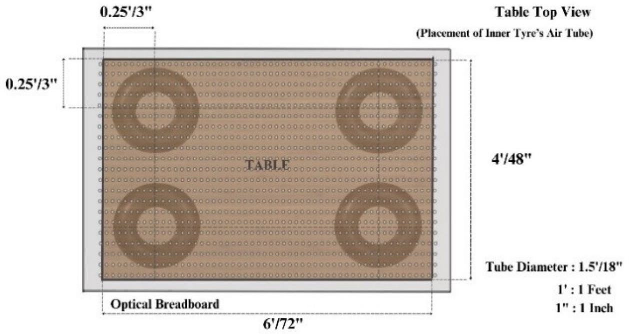

FIG. 11(a): Placement of air tubes below the optical breadboard.

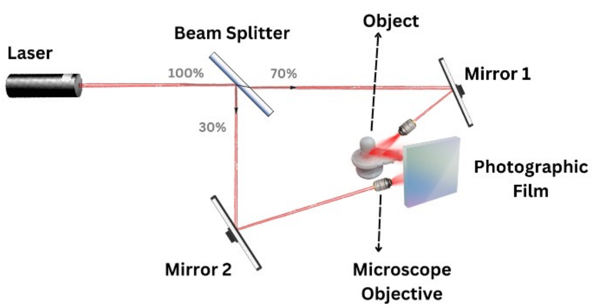

FIG. 11(b): Schematic view of the setup of the construction of the hologram.

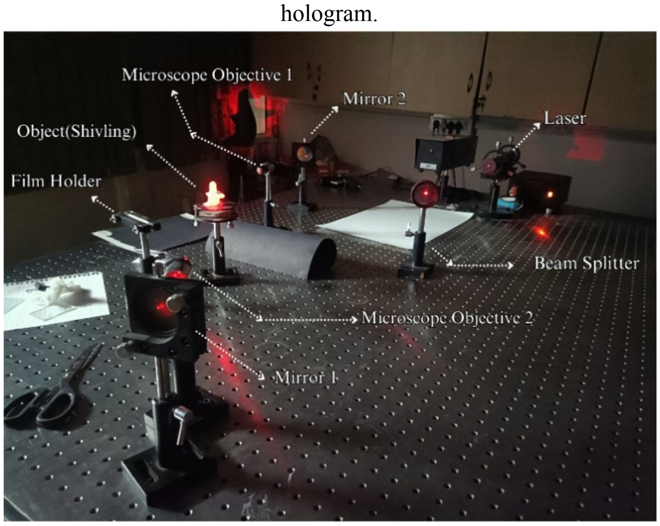

FIG. 12: Actual setup on the optical breadboard.

2.2.2 Methodology of Construction of Hologram

A. ***Setup for Recording***

1. Arrange the four air tubes with air pressure 20 psi at the four corners of the optical breadboard (Fig. 11(a)) to ensure the required vibration isolation.
2. Carefully arrange all components /instruments as shown in Figure 11(b). All the components shall be firmly fixed on the optical breadboard using M6 screws. We should use the glue gun to ensure that the object is fixed on the object table. Glue gun can be used at different places to reduce the probability of vibrations.
3. It is very important to make path length of the object beam approximately equal to the path length of the reference beam.
4. Switch on the laser at least half an hour before recording hologram, so that its output power is stabilized.
5. It is to be made sure that the object beam is maximally illuminating the object. The scattered beam from the object and the magnified reference beam are both overlapping on the dummy screen mounted at the place where photographic film will be mounted.
6. Once the above requirements are fulfilled, block the laser beam by placing a black cardboard sheet in front of it.

B. ***Prerequisites before starting recording***

1. Turn off all unnecessary lights in the lab to minimize background light interference.
2. Unwrap the photographic film and use a scissor to cut it into square pieces, also make a small cut on the top right side of the film so that in the future you will know which side was placed in front and which one in back.
3. Sandwich the film between a cleaned set of glass plates. Clamp the glass plates sandwiching the photographic film with paper clip.
4. Replace the dummy screen by the sandwiched photographic film.
5. Continue to block the laser beam using a black cardboard sheet directly in front of its opening. Leave the optical breadboard undisturbed for at least one minute to let vibrations (if any) settle.
6. After the settling period is over, carefully lift the black sheet without moving it away from the laser. Hold it with your hands in front of the beam such that it still blocks the laser beam without touching the table.
7. Wait for another forty-five seconds for any vibrations to fully settle down.

C. ***Recording***

1. The intensity of the reference beam should be four to five times more than the object beam, measured at the recording plane. A cardboard piece in L-shape may be used as shutter by first gently lifting it slightly above the table for few seconds and then removing for an exposure of (say) 60 seconds.
2. During this crucial exposure time, one must be extremely careful not to disturb the optical breadboard in any way including:
   a. Avoid vibrations from phones or any other electronic gadget.
   b. Don't blow air including your breath towards the table.
   c. Do not touch the optical breadboard/table on which it is kept or its components
3. It is to be noted that even miniscule variation in the path length caused by vibrations can affect the quality of the interference pattern which is recorded on the photographic film.
4. The exposed film can be kept in black envelope before development.
5. The actual set-up in the dark room is as shown in Fig. 13

It is to be noted that for making high efficiency holograms we need to use spatial filters in place of microscope objectives and shutter for proper time of laser beam exposure.

Figure 13. Photo of the Hologram recording Setup in the dark.

D. ***Photographic Film Development***

1. All the film processing has to be done in green safe light.
2. We have used Kodak D-76 developer (packet supplied by Kodak company). The method of preparation of Kodak D-76 developer solution is printed on the packet. 10% Sodium thiosulphate (commonly called hypo) solution is prepared for fixing the image on photographic film. Generally, we use distilled water for making our developer. We can also use deionised water for making the developer.
3. Take three different plastic trays. Put the developer solution in the first tray, Fixer solution in the second tray, and Normal tap water in the third.

4. Take out the exposed photographic film from the black envelope, dip the film in the first tray containing the developer solution and gently move the tray back and forth slowly and evenly to cause the solution to move continuously over the film. Develop the film for six minutes. The development time can be different depending upon which developer solution is being used.
5. After development, wash the film in the third tray for two minutes.
6. Now put the film into the second tray containing the fixer solution and fix the film for five minutes.
7. Wash the film for another three minutes in the third tray and then wash the film for one minute in running water.
8. Dry the film manually by moving it back and forth in air by holding it in your hand. One should avoid the use of a hot air blower or any kind of hot air source to dry it, as it can damage the recorded interference pattern.

E. ***About Developer Solution and Fixer***

We have used Kodak D-76 Developer for preparing the Developer solution and Sodium Thiosulphate Solution as Fixer for high-resolution photography. The details about development time etc., one can refer to Kodak Developer D-76 [19].

2.2.3 Setup Diagram for Reconstruction of Hologram.

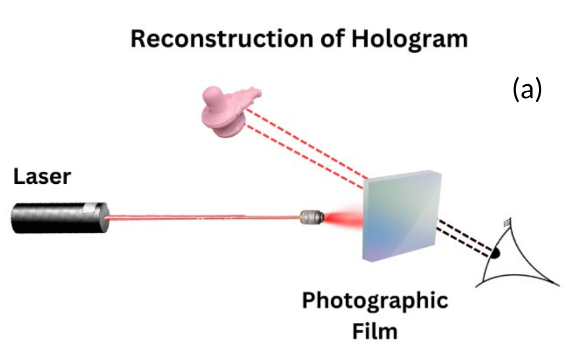

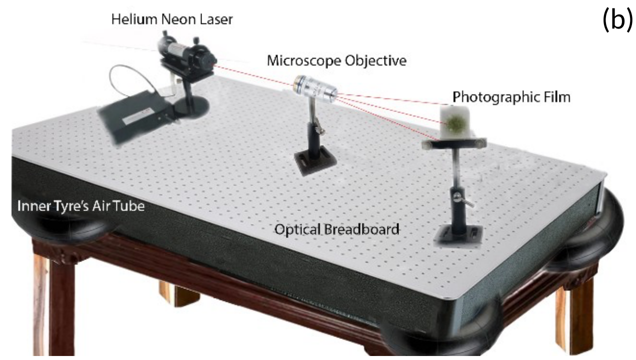

Figure 14. (a) Schematic view of the setup of the reconstruction of the hologram. **(b)** Setup on the optic table.

The schematic of the set-up for reconstruction of the recorded hologram is as shown in Figure 14.

2.2.4 Methodology of Reconstruction of Hologram.

1. ***Setup for Reconstruction:***

Arrange the developed holographic film/plate, laser light source, and microscope objective in the identical configuration used for the initial recording process (as shown in Figure 14).

2. ***Reconstruction of Wavefront:***

When the reference beam is incident on the hologram then the diffracted light from the holographic plate reconstructs the original wavefront that was present when the hologram was recorded.

3. ***Formation of 3D Image:***

1. A 3D image of the object is formed in the space where the original object or scene was located during the holographic recording. This is called virtual image of the object.
2. We can easily see that two images will be formed, the first one is a REAL image which is seen towards the observer (-1 Order), and the second one is a VIRTUAL

image which is behind the photographic film (1 Order) (Figure 15).

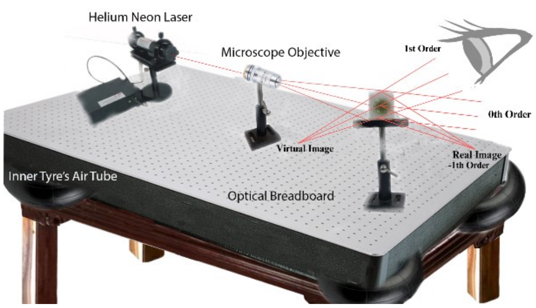

Figure 15. Reconstruction of Holograms with image formation with their positions.

3. Results.

In the present paper, we have explained about the systematic approach for successful recording and reconstruction of holograms in a cost-effective manner at undergraduate level. Notably, due to the intricate equipment and sensitive setup involved, meticulous execution is crucial for achieving clear and accurate holographic recordings. Fig. 16 shows the successfully recorded and developed holographic films.

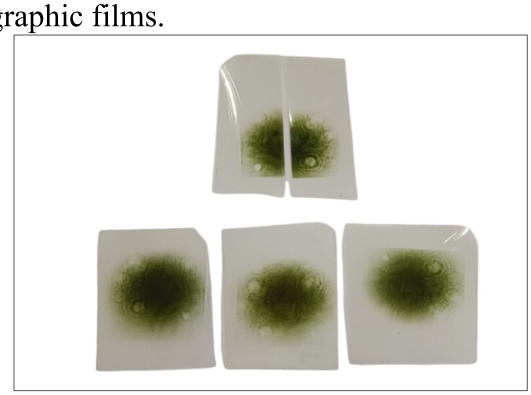

FIG. 16: Successfully recorded Holograms (Photographic films).

The reconstructed images of the holograms with object as Shivling are as shown in Fig. 17(a) and 17(b).

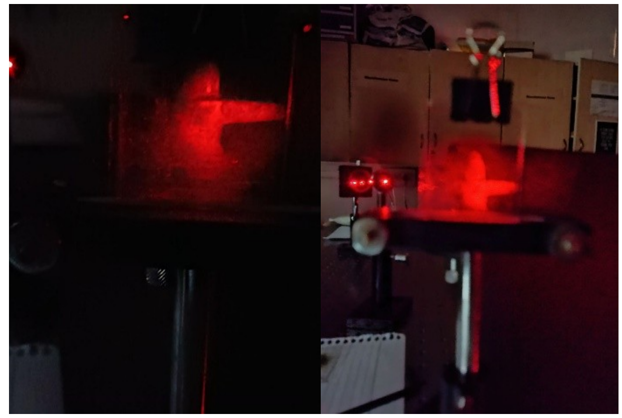

(a) **(b)**

FIG. 17: **(a)** A close-up view of the image formed on the Photographic film. **(b)** A sandwiched hologram film between glass plates using a paper clipper.

While the experiment presented certain challenges due to the potential for error and subsequent failure in generating high-quality holograms, careful procedures and close attention to detailed procedure allowed for five successful consecutive recordings.

4. Discussion.

Ensuring a vibration-free environment poses a critical challenge in this experiment, as even minute vibrations can disrupt the laser beam's path length, irreversibly distort the interference pattern and thus render an unsuccessful recording of the hologram. Traditional vibration isolation methods often rely on specialized equipment, leading to considerable cost constraints in research and development projects [20,21]. This study presents a unique solution: leveraging readily available air tubes as a cost-effective substitute for conventional vibration isolators. Surprisingly, our results demonstrate that air tubes offer comparable isolation performance, effectively negating vibrations that could compromise experimental accuracy and data integrity. The key lies in the intrinsic properties of air. By strategically employing air tubes within the experimental setup, we were able to exploit its natural damping characteristics to dissipate unwanted vibrations. This innovative approach not only delivers performance at par with expensive isolators but also unlocks significant cost savings. With readily available materials and simple implementation, air tubes can present a compelling alternative for a wide range of research applications.

Unlike conventional photographs, holograms exhibit remarkable resilience to fragmentation. Cutting a hologram creates miniature complete object replicas, each retaining the full image, albeit with reduced resolution and intensity (Figure 18). This unique property, rooted in the redundant encoding of information, defies the limitations of two-dimensional representations, offering a fascinating glimpse into the world of holographic data storage and retrieval.

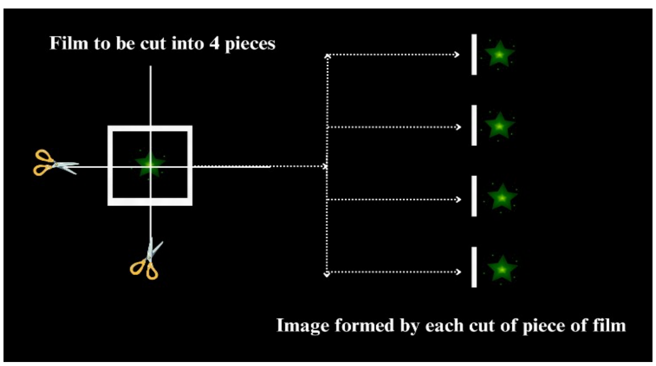

FIG. 18: Represents the retrieval of the original image of the object from each cut slides.

4.1 Cautions

1. Before commencing recording (minimum 30 minutes), deactivate all potential vibration sources within the lab, including air conditioners, exhaust fans, and other equipment generating air movement.
2. Avoid film exposure to any light source until the development stage is complete. Light exposure before development can negatively impact the final holographic image quality in the present case. However, optimized some pre-exposure to white light may be used when the intensity output of the laser light is very low.
3. Refrain from using hot air blowers for drying the photographic film after development. Employ alternate drying methods that are gentle and controlled, preventing damage to the delicate film layer.
4. Maintain cleanliness and meticulous upkeep of all equipment, particularly the glass plates used to sandwich the photographic film. Dust, impurities, or imperfections on these surfaces can affect the recording process and image quality.
5. Always handle the photographic film by the corners. Avoid touching the film surface from anywhere else, as fingerprints or other contaminants can affect the final image quality.

4.2 Importance of the present work

In this paper, a cost-effective and straightforward hologram recording process designed to be accessible even to undergraduate students. By simplifying the complexities traditionally associated with holography, this method opens up new possibilities for experimentation and learning in optics and imaging. This technique utilizes basic optics principles and accessible materials, demonstrating the fascinating world of holography while fostering hands-on learning and experimentation. It combines affordability with educational value, offering a clear pathway for enthusiasts and academics alike to explore the fascinating world of holographic technology. Holographic technology can also be probably used as a motivating and interdisciplinary education strategy. At AND College (University of Delhi) we frequently organize workshop on holography for interacting with undergraduate/graduate/school teachers and students. These efforts have shown that co-operation between university/college and school is very important in order to promote understanding of holography and its applications in education.

5. Conclusion

By successfully mastering the intricacies of holographic recording and reconstruction at an undergraduate level, the present work signifies valuable learning outcomes for undergraduate students including practical exposure to real-world optics experiments. This work showcases a systematic and cost-effective approach to holography, catering specifically to the needs of researchers and students at the undergraduate level. The demonstrated error-free method outlined in this paper not only provides a comprehensive guide that has not been reported so far in this manner but also emphasizes simplicity, affordability, and success in hologram recording and reconstruction.

One of the key strengths of this method is its adaptability. The instructions provided enable users to customize the process according to their specific requirements, promoting creativity and exploration in holography. This adaptability not only supports individual learning but also encourages teamwork, as users can collaborate to refine and enhance the methodology based on their collective experiences.

The emphasis on optics education at the undergraduate level is noteworthy, as it aligns with the growing demand for practical, hands-on learning experiences in science and engineering disciplines. By offering an affordable and easily implementable holography method, this work contributes to a more engaging and enriching educational experience for students. Furthermore, the paper serves as a bridge between theoretical concepts and real-world applications, enhancing the understanding of holography within the academic community.

Acknowledgements

The author would like to thank the Principal, Acharya Narendra Dev College for the infrastructural support and the SPIE Student Chapter at the University of Delhi (ANDC) for providing financial and peer group support for carrying out the studies.

References:

[1] P. Hariharan, *Optical Holography: Principles, Techniques and Applications* (Cambridge University Press, 1996). DOI: 10.1016/B978-0-12-815467-0.00001-3

[2] "The Nobel Prize in Physics 1971," *Nobelprize.org* (1971). (https://www.nobelprize.org/nobel_prizes/physics/laureates/1971/)

[3] E. A. Franke and J. M. Franke, *IEEE Trans. Educ.* **17**, 166 (1974).

[4] P. M. Pombo, R. M. Oliveira, and J. L. Pinto, *Proc. SPIE* **4659**, 109 (2002).

[5] S. G. Paredes and N. R. Vázquez, *Int. J. Interact. Des. Manuf.* **14**, 1321 (2020).

[6] H. Ghuloum, in *Informing Science & IT Education Conference* (Informing Science Institute, Santa Rosa, CA, 2010), p. 693.

[7] A. Ratan, *Holography – Working Principle and Applications* (2015). DOI: 10.13140/RG.2.1.2688.4649

[8] J. T. Sheridan, R. K. Kostuk, A. F. Gil, Y. Wang, W. Lu, H. Zhong, Y. Tomita, C. Neipp, J. Francés, S. Gallego, and I. Pascual, *J. Opt.* **22**, 123002 (2020).

[9] T. H. Jeong, *Basic Principles and Applications of Holography* (Lake Forest College, Lake Forest, Illinois, 2010).

[10] "Filmmaker's Guide to Creating Holograms," *PremiumBeat* (2015).

(https://www.premiumbeat.com/blog/filmmaker-guide-to-creating-holograms/)

[11] G. Saxby and S. Zacharovas, *Holography: Practical Information and Applications* (CRC Press, 2015). ISBN 9781482251579.

[12] J. Salancon *et al.*, *Eur. J. Phys.* 40, 015301 (2019). DOI: 10.1088/1361-6404/aae8ba

[13] Edmund Optics, "Understanding Microscopes and Objectives," *Knowledge Center Application Notes – Microscopy* (2020). (https://www.edmundoptics.in/knowledge-center/application-notes/microscopy/understanding-microscopes-and-objectives/)

[14] Geola, "PFG-01 Holographic Film" (2020). (https://www.geola.com/product/pfg-01-film/)

[15] IndiaMART, "He–Ne Laser Red Beam." (https://www.indiamart.com/proddetail/he-ne-laser-red-beam-2111639755.html)

[16] Wikipedia, "Optical Table." (https://en.wikipedia.org/wiki/Optical_table)

[17] IndiaMART, "Honeycomb Breadboard Optical Table." (https://www.indiamart.com/proddetail/honeycomb-breadboard-optical-table-21380852812.html)

[18] IndiaMART, "Synthetic Rubber Inner Tubes." (https://www.indiamart.com/proddetail/synthetic-rubber-inner-tubes-16588026212.html)

[19] Kodak Alaris, "Imaging Resources, Technical Data J-78." (https://imaging.kodakalaris.com/sites/default/files/files/resources/j78.pdf)

[20] Thorlabs, "Optomechanical Components." (https://www.thorlabs.com/newgrouppage9.cfm?objectgroup_id=1095)

[21] Minus K Technology, "Price List – Vibration Isolators, Tables, Platforms, Benchtops." (https://www.minusk.com/content/price-list_vibration_isolators_table_platforms_benchtops.html)

Numerical Simulation and Chaos Characterization of a Double Pendulum with Magnetic Damping

Ankush Chakrabarty[1] and Dr. Parimal Sarkar[1]

[1]Department of Physics, Coochbehar College, Coochbehar 736101, India.

Submitted on 03-09-2025
Accepted on 13-04-2026

Abstract

This paper investigates the nonlinear dynamics of a planar double pendulum subjected to a magnetic (eddy-current-type) damping torque acting on each bob. Starting from the Lagrangian, we derive the coupled equations of motion including the damping torques, reduce them to an explicit closed-form first-order system, and integrate them numerically with a fourth-order Runge–Kutta scheme across three damping strengths ($k_m = 0$, 0.05, and 0.3 N·m·s). Time series, phase portraits, Poincaré sections, energy decay, and finite-time maximal Lyapunov exponent estimates are used together, rather than in isolation, to characterize the qualitative transition from chaotic to regular dynamics as damping increases. We report this transition cautiously: the finite-time Lyapunov estimate at $k_m = 0$ is slightly negative even though the corresponding Poincaré section and phase portraits are visibly chaotic, a known artefact of short integration windows in weakly chaotic systems, and we treat the multi-diagnostic qualitative trend — not any single numerical exponent — as the reliable result. We connect the phenomenological damping coefficient to eddy-current material parameters, explicitly discuss the mathematical equivalence of the present linear damping law to viscous damping and its limits of validity, validate the integrator against energy-conservation and time-step-convergence checks, and outline the scope, limitations, and pedagogical value of the study.

Keywords: Double pendulum, Magnetic (eddy-current) damping, Deterministic chaos, Lyapunov exponent, Poincaré section, Lagrangian mechanics, Nonlinear dynamics education.

Symbol	Meaning
θ_1, θ_2	Angular displacement of bob 1, bob 2 from the vertical
ω_1, ω_2	Angular velocity, $\omega_i \equiv \dot{\theta}_i$
m_1, m_2	Bob masses
L_1, L_2	Pendulum arm lengths
g	Gravitational acceleration
k_m	Magnetic (eddy-current) damping coefficient (assumed equal at both joints)
$\tau_{d,i}$	Damping torque at joint i
$\mathcal{L}, F$	Lagrangian; Rayleigh dissipation function
σ, B, t, A, r	Conductivity, field strength, plate thickness, area, radius (Section 3.2)
γ	Nondimensional damping ratio
M, C, K	Mass, damping, and stiffness matrices of the linearized system (Section 3.5)
Ω_1, Ω_2	Small-oscillation normal-mode frequencies of the linearized system (Section 3.5)
s	Complex growth rate of a linearized normal mode, $\boldsymbol{\theta} \propto e^{st}$ (Section 3.5)
λ	Maximal Lyapunov exponent (Sections 3.6, 6)
T	Total simulated physical time (40 s throughout)
Δt	Integration time step

1 Introduction

The double pendulum is a prototypical system in nonlinear dynamics, displaying behaviours ranging from simple periodic motion to fully developed chaos. Its extreme sensitivity to initial conditions makes it a natural testbed for studying deterministic chaos, both in research and in the classroom.

Dissipation in real systems can arise from viscous drag, mechanical friction, or electromagnetic effects such as eddy-current (magnetic) damping. Magnetic damping is attractive in precision mechanical systems because it is contactless and wear-free, and it can be tuned via magnetic field strength or conductor geometry. This tunability, rather than any exotic mathematical form, is the practical motivation for studying it here.

This paper presents a theoretical derivation and numerical exploration of a double pendulum incorporating magnetic damping, with two aims. First, at the research level, we quantify how the strength of a contactless damping torque reshapes the phase space of a two-degree-of-freedom nonlinear system, using explicit equations of motion together with several complementary chaos diagnostics. Second, at the pedagogical level, we frame the study so that it is directly reproducible in a computational-physics laboratory, with explicit learning outcomes.

We emphasize at the outset — and return to in Section 3.3 — that the damping law adopted here is the standard linear, low-velocity model of eddy-current damping, and that in this regime it is mathematically identical in form to linear viscous damping. The distinguishing physical content of the study is therefore not a new equation of motion in the abstract sense, but the specific combination of a physically motivated, contactless damping mechanism with a systematic, multi-diagnostic chaos characterization of the two-body system, discussed next.

2 Literature Review

Foundational treatments of nonlinear dynamics and chaos, such as those by Strogatz [1] and Moon [2], provide the theoretical backdrop for the present study. Early numerical and experimental investigations of the double pendulum established its chaotic character and sensitivity to initial conditions [3, 4]; Levien and Tan [4] in particular built a physical apparatus and compared measured Poincaré sections against simulation, which is the kind of experimental benchmark that the present, purely numerical study still lacks (see Section 7.3). Stachowiak and Okada [5] carried out a systematic numerical study of the undamped double pendulum using bifurcation diagrams and Lyapunov exponents computed across a range of energies, rather than at isolated parameter values, illustrating the value of a dense parameter sweep — a methodological point we adopt as an explicit item for future work (Section 7.3).

Magnetic (eddy-current) damping has a separate history in single-degree-of-freedom systems, where it is shown to provide smooth, contactless dissipation [6], and it remains an active area of applied research: Polczyński et al. [7] designed and characterized a large-scale eddy-current damper for structural vibration control, and Khomeriki [8] analysed parametric-resonance-induced chaos in a magnetically damped driven pendulum, showing that magnetic dissipation can both suppress and, under parametric forcing, induce chaotic transitions.

More recent work on the double pendulum specifically has emphasized quantitative chaos diagnostics. Hillebrand et al. [9] used Lagrangian descriptors to map the regular and chaotic regions of the double-pendulum phase space, while Cabrera et al. [10] quantified the fraction of phase space occupied by chaotic versus regular motion as a function of energy. Both studies, however, consider the idealized (undamped) double pendulum over a fine energy grid; neither incorporates a physically motivated dissipation mechanism. Conversely, the magnetic-damping studies above are confined to single-degree-of-freedom systems. Literature that combines the two — magnetic damping in a coupled, two-degree-of-freedom chaotic system — remains sparse.

2.1 Positioning Relative to Prior Work

Rather than asserting priority claims outright, we position the present study relative to the specific papers discussed above, and note explicitly where our evidence for a gap is necessarily limited to the literature we have reviewed.

Damped Lagrangian model. The papers on magnetic damping cited above [6, 8, 7] address single pendula or engineering dampers; the double-pendulum chaos papers [3, 5, 9, 10] consider the undamped or viscously damped case. We are not aware of a published closed-form Lagrangian derivation of the double pendulum with an eddy-current-type damping torque at both joints; Section 3.1 provides one.

Coefficient-to-physics link. Existing eddy-current pendulum studies estimate k_m for a single body. Section 3.2 extends the same scaling argument to the two-body case. This is a modest, incremental extension of established eddy-current theory [6, 7] rather than a new physical result.

Multi-diagnostic damping sweep. To our knowledge, no published study reports time series, phase portraits, Poincaré sections, energy decay, and Lyapunov estimates together across a damping sweep for this specific system; prior double-pendulum chaos papers apply a subset of these diagnostics to the undamped case only, and prior magnetic-damping papers report energy or amplitude decay without Poincaré or Lyapunov analysis. We present this combination in Section 5.4, while acknowledging in Section 7.3 that our sweep uses only three damping values, which is sparse compared with the fine energy grids used by Stachowiak and Okada [5] and Cabrera et al. [10].

Implementation notes. Section 4.2 documents specific numerical pitfalls (angle unwrapping, interpolated Poincaré event detection, finite-window Lyapunov bias) that are not discussed in detail in the papers above. We present this as a practical, reusable methodological note rather than a novel algorithm.

Pedagogical framing. Section 7.1 states explicit learning outcomes for classroom use, which is not the purpose of the research-oriented papers cited above.

We stress that these are differences of combination and emphasis relative to the specific papers we have reviewed, not claims of a new physical effect, and we have tried to phrase them so that they can be checked directly against the citations given.

3 Theory and Mathematical Model

Consider two rigid pendula of masses m_1, m_2 and lengths L_1, L_2, connected in series and constrained to move in a vertical plane. Let θ_1 and θ_2 denote the angular displacements of the first and second bobs, measured from the downward vertical.

The Cartesian coordinates of the bobs are

$$x_1 = L_1 \sin\theta_1, \qquad y_1 = -L_1 \cos\theta_1, \quad (1)$$

$$x_2 = x_1 + L_2 \sin\theta_2, \qquad y_2 = y_1 - L_2 \cos\theta_2. \quad (2)$$

The kinetic energy T and potential energy V of the system are

$$T = \frac{1}{2}m_1(L_1\dot\theta_1)^2 + \frac{1}{2}m_2\Big[(L_1\dot\theta_1)^2 + (L_2\dot\theta_2)^2 + 2L_1L_2\dot\theta_1\dot\theta_2\cos(\theta_1-\theta_2)\Big], \quad (3)$$

$$V = -(m_1+m_2)gL_1\cos\theta_1 - m_2gL_2\cos\theta_2, \quad (4)$$

giving the Lagrangian $\mathcal{L} = T - V$. Magnetic damping is modelled as a torque opposing each bob's angular velocity, $\tau_{d,i} = -k_m\dot\theta_i$, with the same coefficient k_m at both joints for simplicity (this simplification is revisited in Section 7.3). This is equivalent to including the Rayleigh dissipation function

$$F = \frac{1}{2}k_m\left(\dot\theta_1^2 + \dot\theta_2^2\right), \qquad \tau_{d,i} = -\frac{\partial F}{\partial\dot\theta_i}, \quad (5)$$

in the Euler–Lagrange equations,

$$\frac{d}{dt}\frac{\partial\mathcal{L}}{\partial\dot\theta_i} - \frac{\partial\mathcal{L}}{\partial\theta_i} = -\frac{\partial F}{\partial\dot\theta_i}. \quad (6)$$

3.1 Explicit Equations of Motion

Differentiating the Lagrangian and substituting into the Euler–Lagrange equations gives the coupled, nonlinear, second-order equations of motion:

$$\begin{aligned}&(m_1+m_2)L_1^2\ddot\theta_1\\ &\quad + m_2L_1L_2\ddot\theta_2\cos(\theta_1-\theta_2)\\ &\quad + m_2L_1L_2\dot\theta_2^2\sin(\theta_1-\theta_2)\\ &\quad + (m_1+m_2)gL_1\sin\theta_1 = -k_m\dot\theta_1, \quad (7)\\ &m_2L_2^2\ddot\theta_2 + m_2L_1L_2\ddot\theta_1\cos(\theta_1-\theta_2)\\ &\quad - m_2L_1L_2\dot\theta_1^2\sin(\theta_1-\theta_2)\\ &\quad + m_2gL_2\sin\theta_2 = -k_m\dot\theta_2. \quad (8)\end{aligned}$$

These can be written as a linear system in the angular accelerations, $A(\theta)\,\ddot{\boldsymbol\theta} = \mathbf{b}(\theta,\dot\theta)$, with $\Delta \equiv \theta_1 - \theta_2$:

The determinant $\det A = m_2L_1^2L_2^2\left[(m_1+m_2) - m_2\cos^2\Delta\right]$ is strictly positive for physical parameters, so the system inverts in closed form via Cramer's rule:

$$\ddot\theta_1 = \frac{A_{22}b_1 - A_{12}b_2}{\det A}, \qquad \ddot\theta_2 = \frac{A_{11}b_2 - A_{21}b_1}{\det A}. \quad (12)$$

For numerical integration these are recast as a four-dimensional first-order sys-

$$A_{11} = (m_1 + m_2)L_1^2, \qquad A_{12} = A_{21} = m_2 L_1 L_2 \cos\Delta, \qquad A_{22} = m_2 L_2^2, \tag{9}$$
$$b_1 = -m_2 L_1 L_2 \dot\theta_2^2 \sin\Delta - (m_1 + m_2) g L_1 \sin\theta_1 - k_m \dot\theta_1, \tag{10}$$
$$b_2 = m_2 L_1 L_2 \dot\theta_1^2 \sin\Delta - m_2 g L_2 \sin\theta_2 - k_m \dot\theta_2. \tag{11}$$

tem in $(\theta_1, \omega_1, \theta_2, \omega_2)$. The closed-form matrix inversion, rather than a fixed symbolic expansion, is used because it remains exact for arbitrary m_1, m_2, L_1, L_2 and avoids algebra errors that commonly arise when hand-expanding these equations.

3.2 Physical Basis and Estimation of the Magnetic Damping Coefficient

The linear torque law $\tau_d = -k_m\dot\theta$ is the standard low-velocity model for eddy-current damping [6]. A conducting element of thickness t and area A moving with speed v through a field B experiences a retarding force $F \approx \sigma B^2 t A v/\rho_m$, where σ is the electrical conductivity and ρ_m a geometric resistance factor of the induced current loops. For a pendulum bob at radius r from the pivot, this gives a damping torque $\tau_d \approx (\sigma B^2 t A r^2/\rho_m)\dot\theta$, i.e. $k_m \propto \sigma B^2 t A r^2$, consistent with the eddy-current damper characterization of Polczyński et al. [7].

In the present simulations, $k_m = 0$, 0.05, and 0.3 N·m·s are intended to bracket the undamped, weak-eddy-current, and strong-eddy-current regimes achievable with benchtop permanent magnets and aluminium or copper vanes. The corresponding nondimensional damping ratio (Section 3.4) is $\gamma \approx 0$, 0.05, and 0.3.

3.3 Relationship to Viscous Damping and Scope of the Damping Model

It is important to be explicit about a point raised in review: the torque law $\tau_d = -k_m\dot\theta$ used throughout this paper is, as a piece of mathematics, identical in form to linear viscous (Stokes) damping. The physical distinction lies not in the equation but in the mechanism generating it — induced eddy currents rather than fluid drag or dry friction — which is what makes the coefficient k_m continuously and remotely tunable via field strength or magnet–conductor gap, without mechanical contact or wear. This tunability, not a novel damping functional form, is the applied motivation for the model.

The linear law is only the low-velocity limit of true eddy-current damping. At higher angular velocities, the spatial distribution of induced currents and the resulting torque can become nonlinear (e.g. scaling closer to $\dot\theta^2$ at high speed, or saturating as induced fields begin to oppose the source field). The present study does not model this regime; a velocity-dependent $k_m(\dot{\theta})$ is identified as a concrete extension in Section 7.3.

3.4 Non-dimensionalization

Introducing the characteristic length $L = L_1$ and time scale $T_0 = \sqrt{L/g}$, we define nondimensional time $\tau = t/T_0$ and nondimensional damping $\gamma = k_m/(mL^2/T_0)$, where m is a representative mass scale. This allows the results to be generalized to different physical scales. Results are reported in dimensional form throughout for direct interpretability, with γ provided for cross-reference with other studies.

3.5 Linear Stability Analysis of the Equilibria

Setting $\dot{\theta}_i = \ddot{\theta}_i = 0$ in Eqs. (7)–(8) gives $\sin\theta_1 = \sin\theta_2 = 0$, so the system has four equilibrium configurations (mod 2π): $(0,0)$, $(0,\pi)$, $(\pi,0)$, and (π,π), corresponding to every combination of each bob hanging down or balanced inverted. We linearize about the physically relevant downward equilibrium $(0,0)$, writing θ_1,θ_2 as small and retaining first-order terms only, so $\sin\theta_i \approx \theta_i$, $\cos(\theta_1-\theta_2) \approx 1$, and the velocity-squared terms in Eqs. (7)–(8) (already second order) vanish. This gives the linear system

$$M\ddot{\boldsymbol{\theta}} + C\dot{\boldsymbol{\theta}} + K\boldsymbol{\theta} = \mathbf{0}, \qquad (13)$$

with $\boldsymbol{\theta} = (\theta_1,\theta_2)^{\mathsf{T}}$. Seeking normal-mode solutions $\boldsymbol{\theta} = \boldsymbol{\theta}_0 e^{st}$ gives the characteristic equation $\det(Ms^2 + Cs + K) = 0$, a quartic in s.

Undamped case ($k_m = 0$). Setting $s = i\Omega$ reduces this to the classical small-oscillation secular equation $\det(K - \Omega^2 M) = 0$, which expands to

$$\mathrm{m}_1 L_1 L_2\,\Omega^4 - (m_1+m_2)g(L_1+L_2)\,\Omega^2 + (m_1+m_2)g^2 = 0, \ (15)$$

with two positive roots

For the equal-mass, equal-length case ($m_1 = m_2 = m$, $L_1 = L_2 = L$), Eq. (16) reduces to the textbook result $\Omega^2_{1,2} = (2 \pm \sqrt{2})g/L$ [1], which we use as an internal check on Eq. (16). Both roots are real and positive for all physical $m_1, m_2, L_1, L_2 > 0$, so in the undamped limit $(0,0)$ is a centre (marginally stable, surrounded by closed orbits in the linearized system) rather than a spiral or saddle. By the same construction, linearizing about either single-inverted equilibrium, $(\pi,0)$ or $(0,\pi)$, flips the sign of the corresponding diagonal entry of K, which makes $\det(K - \Omega^2 M) = 0$ admit an imaginary root and identifies that equilibrium as a saddle (unstable); (π,π) is likewise unstable. This is consistent with never observing the trajectories in Section 5 approach an inverted configuration.

Damped case ($k_m > 0$). With $C = k_m I \neq 0$, the quartic $\det(Ms^2 + Cs + K) =$

$$\Omega_{1,2}^2 = \frac{(m_1+m_2)g(L_1+L_2) \pm g\sqrt{(m_1+m_2)\left[(m_1+m_2)(L_1+L_2)^2 - 4m_1L_1L_2\right]}}{2m_1L_1L_2}. \tag{16}$$

0 has four roots with strictly negative real part for any $k_m > 0$ (a Routh–Hurwitz argument on the quartic, or equivalently the standard result that adding positive-definite linear damping to a stable linear oscillator turns centres into stable spirals), so $(0,0)$ becomes asymptotically stable. This is the linear-theory counterpart of the numerical observation in Section 5.3 that all trajectories at $k_m = 0.3$ decay to rest: the linearization correctly predicts *that* the system must eventually settle at $(0,0)$ for any $k_m > 0$, though it says nothing about the strongly nonlinear, large-amplitude chaotic transient that precedes settling, which is why the full nonlinear diagnostics of Section 5–6 remain necessary.

3.6 Lyapunov Exponents: Definition and Interpretation

For a dynamical system $\dot{\mathbf{x}} = \mathbf{f}(\mathbf{x})$ with $\mathbf{x} \in \mathbb{R}^n$ (here $n = 4$, $\mathbf{x} = (\theta_1, \omega_1, \theta_2, \omega_2)$), consider two trajectories separated at $t = 0$ by an infinitesimal vector $\delta(0)$. The Lyapunov exponent associated with that initial perturbation direction is

$$\lambda = \lim_{t\to\infty} \lim_{|\delta(0)|\to 0} \frac{1}{t} \ln \frac{|\delta(t)|}{|\delta(0)|}. \tag{17}$$

In general there is a full spectrum of n exponents $\lambda_1 \geq \lambda_2 \geq \cdots \geq \lambda_n$, one for each independent direction in the tangent space (Oseledets' theorem); by Liouville's theorem their sum equals the average rate of phase-space volume contraction, which is zero for a Hamiltonian (energy-conserving) system and strictly negative for a dissipative system such as the present damped pendulum ($k_m > 0$) [11, 1]. A generic initial perturbation aligns with the fastest-growing direction, so numerically integrating a single perturbed trajectory alongside a reference one, as described operationally in Section 4.2–4.3, estimates only the *maximal* exponent $\lambda \equiv \lambda_1$, which is what is reported in Section 6.

The sign of λ is the standard operational criterion for chaos: $\lambda > 0$ indicates exponential sensitivity to initial conditions (a positive maximal exponent is widely used as sufficient evidence of chaos, though not part of any single necessary-and-sufficient definition); $\lambda = 0$ indicates neutral, quasi-periodic separation (motion confined to an invariant torus, Section 3.7); and $\lambda < 0$ indicates convergence, either to a fixed point or to a stable limit cycle. Two caveats matter for the present study. First, Eq. (17) is defined as a double limit ($t \to \infty$ then $\delta_0 \to 0$), whereas any numerical estimate necessarily uses finite t and finite δ_0; the resulting finite-window bias, already flagged as an implementation issue in Section 4.2, is the theoretical reason the $k_m = 0$ estimate in Section 6 can come out slightly negative despite visibly chaotic phase portraits. Second, for a dissipative system the sum of all exponents is negative even when the maximal exponent λ_1 is positive (the volume contraction is carried by the more negative $\lambda_2, \lambda_3, \lambda_4$), so a positive λ_1 and an overall volume-contracting, attractor-forming flow are not in conflict; this is exactly the structure expected at weak damping in Section 5.2.

3.7 Poincaré Sections and the KAM Theorem

A Poincaré section reduces a continuous flow to a discrete map by recording the state only at successive transversal crossings of a fixed surface Σ in phase space — here, crossings of $\theta_1 = 0$ with a fixed sign of ω_1 (Section 4.2), which reduces the four-dimensional flow to a sequence of points in the $(\theta_2 \bmod 2\pi,\ \omega_2)$ plane. This dimensional reduction is what makes the qualitative structure of an otherwise four-dimensional trajectory visible in a two-dimensional plot.

The relevance of the Poincaré section to the present study rests on the Kolmogorov–Arnold–Moser (KAM) theorem. For a Hamiltonian (undamped, $k_m = 0$) system close to integrable, $H = H_0 + \epsilon H_1$ with ϵ small, the unperturbed system H_0 (e.g. the linearized double pendulum of Section 3.5, whose two normal modes act as action-angle coordinates) has phase space foliated by invariant tori, and a Poincaré section of such a system shows smooth closed curves — the intersections of surviving tori with Σ. The KAM theorem states that for sufficiently small ϵ, invariant tori with sufficiently irrational (Diophantine) frequency ratios survive, only slightly deformed, while tori with rational (resonant) frequency ratios are destroyed and replaced by alternating chains of stable and unstable periodic orbits (Poincaré–Birkhoff theorem), with a thin layer of chaotic motion around the unstable ones [11, 1]. As ϵ grows — physically, as the double pendulum is driven to larger amplitude, further from the small-oscillation regime of Section 3.5 — these chaotic layers widen and overlap (the Chirikov resonance-overlap mechanism), progressively destroying surviving tori until chaos dominates the accessible phase space.

The large-amplitude initial condition used throughout this paper ($\theta_1(0) = 120°$) is deliberately far from the small-oscillation regime of Section 3.5, placing the undamped system deep in this large-ϵ, non-KAM regime rather than near-integrable; this is the theoretical reason the $k_m = 0$ Poincaré section (Figure 2c) is scattered and space-filling rather than composed of smooth curves. Two caveats apply when connecting this theory to the damped cases. First, KAM theory in its standard form applies to conservative (Hamiltonian) systems; for $k_m > 0$ the flow is dissipative, phase-space volume contracts (Section 3.6), and invariant tori are not preserved even approximately in the strict KAM sense — trajectories are instead drawn toward a lower-dimensional attractor, consistent with the stable spiral equilibrium identified in Section 3.5. Second, despite this, weak damping does not destroy the underlying conservative structure instantaneously: for $k_m = 0.05$ the system spends many oscillation periods decaying slowly relative to its natural period, so the trajectory transiently explores a region of phase space still organized by remnants of the undamped system's resonance structure before dissipation dominates, which is consistent with the partial clustering (rather than either fully scattered or fully collapsed structure) seen in the $k_m = 0.05$ Poincaré section (Figure 4c). At $k_m = 0.3$, dissipation dominates on a timescale comparable to the oscillation period itself, and the section collapses rapidly to the stable equilibrium (Figure 6c) with no visible intermediate structure.

4 Numerical Methodology

The equations of motion (Section 3.1) are integrated with a fixed-step fourth-order Runge–Kutta (RK4) scheme. Initial conditions for the primary results are $\theta_1(0) = 120°$, $\theta_2(0) = -10°$, with zero initial angular velocities, placing the system well into the chaotic energy range for the undamped case. Simulations run for $T = 40$ s with $\Delta t = 0.01$ s, for $k_m = 0$, 0.05, and 0.3 N·m·s.

4.1 Numerical Validation

Two checks were performed. *Energy conservation*: for $k_m = 0$, total mechanical energy should be conserved exactly; the RK4 solution shows a fractional drift of less than 0.1% over 40 s (Figure 1b), attributable to the finite time step, confirming $\Delta t = 0.01$ s is adequately small. *Time-step convergence*: halving Δt to 0.005 s changes the estimated maximal Lyapunov exponent by less than 3% for all three damping strengths.

4.2 Simulation Specifications and Implementation Notes

The simulation is written in Python 3 (NumPy, Matplotlib); RK4 is implemented directly in under 30 lines of code, with a typical 40 s trajectory running in well under one second on a standard laptop. Four practical issues arose during implementation.

Angle unwrapping. Because θ_2 can wind through many full rotations in the undamped case, Poincaré sections are computed on θ_2 mod 2π rather than the raw unwrapped angle.

Poincaré event detection. Crossings of θ_1 through zero (fixed sign of ω_1) are located by linear interpolation between adjacent RK4 steps rather than nearest-sample rounding.

Lyapunov estimation. A Benettin-type method integrates a reference and a perturbed trajectory (initial separation $\delta_0 = 10^{-10}$ rad) side by side, periodically renormalizing to avoid overflow and averaging the log-growth rate over renormalization intervals.

Finite-window bias. Because the system is only weakly chaotic at $k_m = 0.05$ and 0.3, the finite-time Lyapunov estimate is sensitive to the renormalization interval and total integration time; values here are indicative of sign and order of magnitude rather than asymptotically converged exponents (Section 7.3).

4.3 Recommended Additional Validation

Beyond the checks in Section 4.1, we explicitly note — rather than leave implicit — three further validation steps that a definitive, publication-grade numerical study of this system should include, and that this manuscript does not yet perform: (i) cross-checking the fixed-step RK4 trajectories against an independent, adaptive-step solver (e.g. an embedded Dormand–Prince RK45 scheme) to bound integration error independently of the RK4 assumption itself; (ii) extending the integration window well beyond 40 s, with ensemble-averaged Lyapunov estimates over many initial-condition pairs, to obtain asymptotically converged exponents rather than the finite-window estimates reported here; and (iii) repeating the full diagnostic suite for multiple mass/length combinations and initial conditions, rather than the single configuration used throughout this paper (see Section 7.3).

5 Results

This section presents time series, phase portraits, energy decay, and Poincaré sections for each damping strength, followed by a comparison across regimes. A note on energy scales: the undamped case (Figure 1b) is plotted as absolute total mechanical energy in Joules, on a scale set by the arbitrary height reference in V, so that the sub-0.1% numerical drift is visible; the two damped cases (Figures 3b and 5b) are plotted as energy relative to their value at $t = 0$, $\Delta E(t) = E(t) - E(0)$, because the dissipated energy (tens of Joules) is what is physically meaningful there, not the absolute offset inherited from the reference height.

5.1 Results for $k_m = 0.0$ (Undamped)

With the large-amplitude initial condition used throughout ($\theta_1(0) = 120°$), the undamped system is driven far from the small-oscillation regime analyzed in Section 3.5, placing it in the strongly non-integrable, large-perturbation regime discussed in Section 3.7. Figure 1 shows the resulting irregular, winding angular motion together with the $< 0.1\%$ numerical energy drift used as a validation check in Section 4.1.

As anticipated in Section 3.7, the Poincaré section (Figure 2c) shows no trace of the smooth invariant curves expected of a near-integrable, KAM-dominated system; the scattered, space-filling pattern is consistent with resonance overlap having destroyed essentially all invariant tori at this

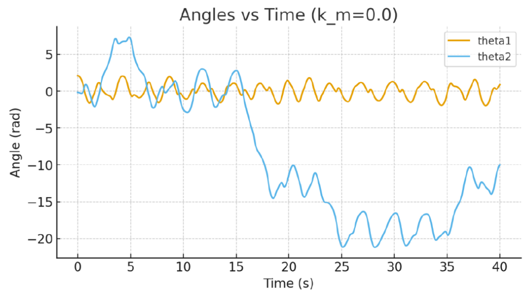

(a) Angular displacements $\theta_1(t)$, $\theta_2(t)$.

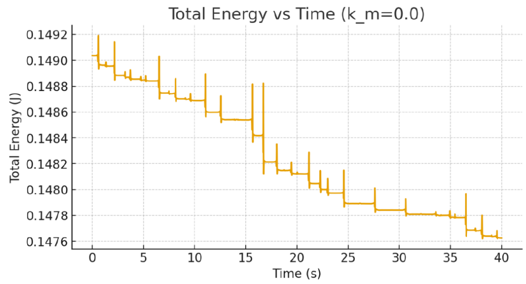

(b) Total mechanical energy (absolute scale; see note above).

Figure 1: Time-domain behaviour for $k_m = 0$. θ_2 winds through many full rotations (a), a hallmark of the large-amplitude chaotic regime; the $< 0.1\%$ energy drift in (b) is a numerical, not physical, effect (Section 4.1).

energy.

5.2 Results for $k_m = 0.05$ (Moderate Damping)

The partial clustering visible in Figure 4c is consistent with the weak-damping picture of Section 3.7: dissipation is slow enough that the trajectory still spends many oscillation periods organized by remnants of the undamped resonance structure before it is drawn toward the stable equilibrium identified in Section 3.5.

5.3 Results for $k_m = 0.3$ (Strong Damping)

This rapid collapse to a point in Figure 6c is the numerical counterpart of the linear stability result of Section 3.5: for any $k_m > 0$ the downward equilibrium $(0, 0)$ is asymptotically stable, and at $k_m = 0.3$ the damping timescale is short enough that this linear prediction dominates the visible dynamics almost immediately, leaving little trace of the chaotic transient seen at weaker damping.

5.4 Comparative Summary Across Damping Strengths

Table 1 collects the quantitative diagnostics for the three damping strengths studied. We emphasize the qualitative, monotonic trend across the table rather than the precise numerical value of λ at any single point: energy-dissipation rate and Poincaré-section confinement both increase monotonically with k_m, while the Lyapunov estimate becomes smaller and eventually changes character.

Table 1: Comparative diagnostics across damping strengths (Section 5).

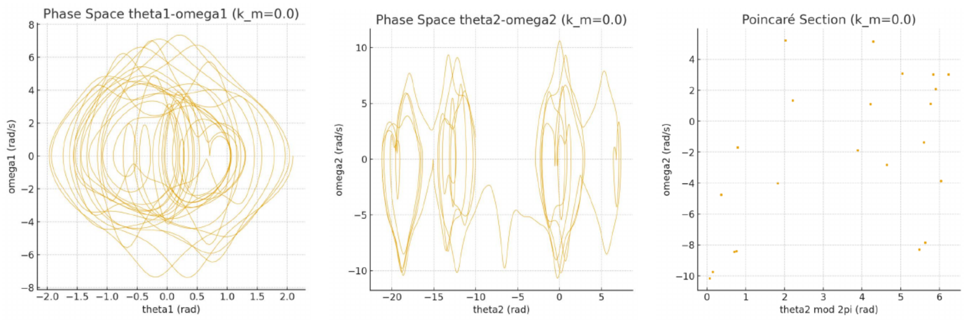

(a) (θ_1, ω_1) (b) (θ_2, ω_2) (c) Poincaré section

Figure 2: Phase-space structure for $k_m = 0$: both bobs fill a broad, non-repeating region of phase space (a,b), and the Poincaré section (c) is scattered and space-filling, consistent with a chaotic attractor.

Diagnostic	$k_m = 0$	$k_m = 0.05$	$k_m = 0.3$
Energy lost over 40 s	$\approx$ 0.001 J (drift only)	$\approx$ 24.5 J	$\approx$ 29.3 J (settles $\sim$15 s)
Poincaré section	Scattered / space-filling	Partially clustered	Collapsed to small region
Maximal Lyapunov estimate λ (s^{-1})	$\approx -0.0213^*$	$\approx +0.0032$	$\approx +0.0006$
Qualitative behaviour	Sustained chaotic wandering	Chaotic transient $\rightarrow$ slow decay	Damped oscillation $\rightarrow$ rest

*Finite-window artefact; not evidence of regularity given the visibly chaotic Poincaré section and phase portraits at $k_m = 0$ (Section 6).

The one apparent inconsistency — a slightly negative λ at $k_m = 0$, the case with the most visibly chaotic phase portraits and Poincaré section — is discussed in Section 6 and should be read as a limitation of the finite 40 s estimation window, not as evidence that the undamped case is regular. Read together with the theoretical picture of Sections 3.5–3.7, the trend in Table 1 has a consistent explanation rather than being a purely empirical curve fit. At $k_m = 0$ the conservative system is driven far into the large-amplitude, non-KAM regime of Section 3.7, so trajectories explore a space-filling chaotic sea with no stable attractor other than the (here irrelevant) linear stability result of Section 3.5. At $k_m = 0.05$, dissipation is weak enough that the system remains organized by remnants of this chaotic structure for many oscillation periods, producing the intermediate, partially clustered Poincaré section, before the asymptotic sta-

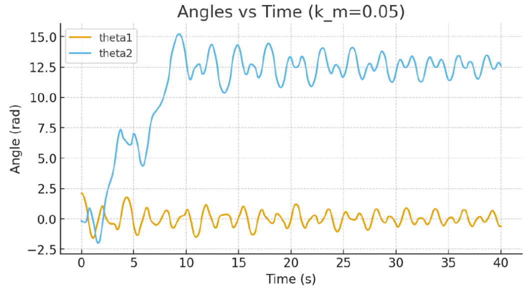

(a) Angular displacements $\theta_1(t)$, $\theta_2(t)$.

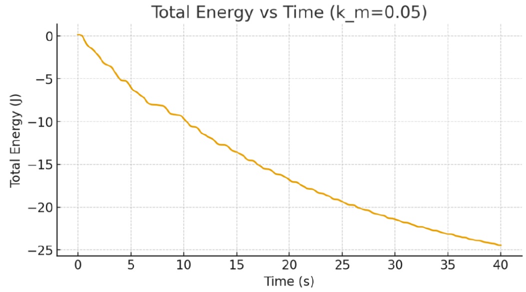

(b) Energy relative to $t = 0$, $\Delta E(t)$ (see note above).

Figure 3: Time-domain behaviour for $k_m = 0.05$: steady, near-linear energy loss accompanies the still-irregular angular motion.

bility of $(0, 0)$ established in Section 3.5 eventually wins out. At $k_m = 0.3$, the damping timescale is short enough relative to the natural oscillation period that the linear stability result dominates almost immediately, collapsing the Poincaré section to a small neighbourhood of the equilibrium well within the 40 s simulation window. The three diagnostics in Table 1 — energy loss, Poincaré confinement, and the (appropriately caveated) Lyapunov estimate — therefore each independently track the same underlying competition between chaotic mixing and linear stabilization, which is the central physical result of this paper.

6 Lyapunov Exponent Estimation

Maximal Lyapunov exponents were estimated with the Benettin-type method of Section 4.2, implementing the formal definition and finite-window caveats given in Section 3.6.

Across all three cases, $|\lambda|$ is small relative to the natural oscillation frequency $\omega_0 = \sqrt{g/L_1} \approx 3.1$ rad/s. We interpret this as reflecting the short 40 s integration window relative to the timescale needed for asymptotic Lyapunov convergence in a weakly chaotic, strongly damped system, rather than as a statement that any of the three cases is truly non-chaotic. The negative estimate at $k_m = 0$ is the clearest illustration of this: it disagrees with the space-filling Poincaré section of Figure 2c, and we treat the Poincaré/phase-portrait evidence as the more reliable indicator at this damping level, consistent with the recommendation in Section 4.3 that Lyapunov estimates from a single finite window should not be relied upon in isolation.

7 Discussion

The results indicate a monotonic trend across the diagnostics in Table 1: with no damping, the system displays sustained chaotic behaviour (irregular, winding time series; broad phase portraits; scattered Poincaré section). With moderate damping, chaotic features persist over the simulated window, but energy decays steadily and the Poincaré section begins to cluster.

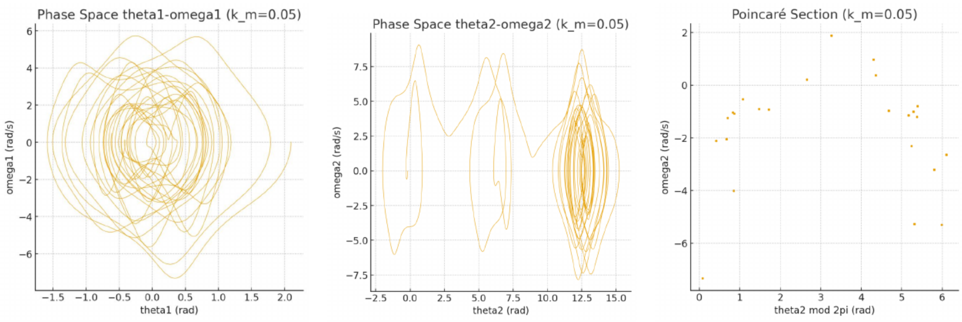

(a) (θ_1, ω_1) (b) (θ_2, ω_2) (c) Poincaré section

Figure 4: Phase-space structure for $k_m = 0.05$: trajectories remain broad (a,b) but the Poincaré section (c) begins to cluster relative to the undamped case.

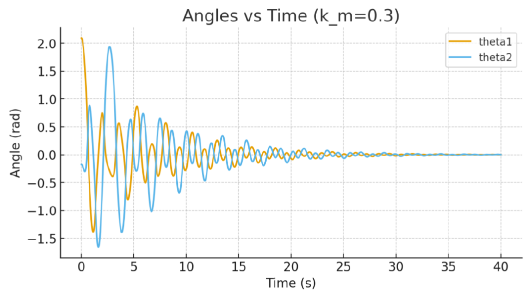

(a) Angular displacements $\theta_1(t)$, $\theta_2(t)$.

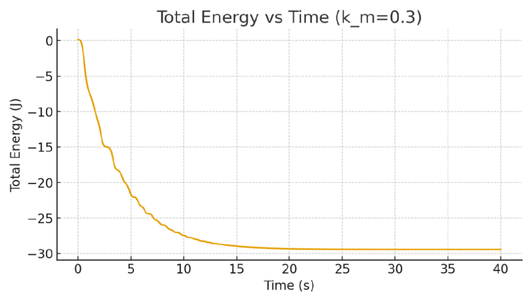

(b) Energy relative to $t = 0$, $\Delta E(t)$ (see note above).

Figure 5: Time-domain behaviour for $k_m = 0.3$: rapid decay to rest within about 20 s, with energy asymptoting to the potential-energy minimum.

With strong damping, the motion rapidly loses energy and settles into a regular, decaying oscillation at the stable equilibrium.

Relative to the viscously damped double pendulum [3], the magnetic damping law used here produces a qualitatively similar chaos-to-order transition. As emphasized in Section 3.3, this is expected given the mathematical equivalence of the two damping laws at low velocity; the practical difference is that magnetic damping strength can be adjusted continuously and remotely, without contact wear, which is the property that motivates eddy-current braking in precision vibration control [7].

7.1 Learning Outcomes for Classroom Implementation

This study supports the following learning outcomes for undergraduate and postgraduate students.

Chaos suppression. Students observe how a single tunable parameter can move a nonlinear system from sustained chaotic wandering to a regular trajectory.

Energy dissipation and its mechanisms. The exercise distinguishes physical dissipation from numerical drift (Section 4.1), an important distinction in computational physics.

Sensitivity to initial conditions. The Lya-

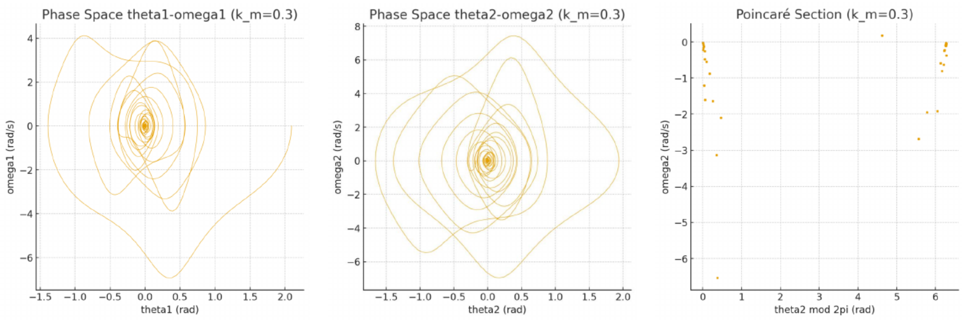

(a) (θ_1, ω_1) (b) (θ_2, ω_2) (c) Poincaré section

Figure 6: Phase-space structure for $k_m = 0.3$: both phase portraits (a,b) spiral into a fixed point and the Poincaré section (c) collapses to a small region.

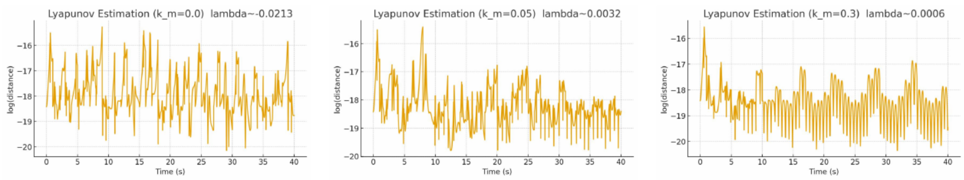

(a) $k_m = 0$ (b) $k_m = 0.05$ (c) $k_m = 0.3$

Figure 7: Log-divergence between two initially nearby trajectories, $\delta_0 = 10^{-10}$ rad. Estimated slopes: $\lambda \approx -0.0213, +0.0032, +0.0006\ \mathrm{s}^{-1}$ respectively.

punov exercise gives hands-on experience with the operational definition of chaos, including the practical subtleties of estimating it numerically.

Diagnostic literacy. Working through several diagnostics side by side teaches that no single one is sufficient alone — directly illustrated by the disagreement between λ and the Poincaré section at $k_m = 0$ (Section 6).

These map onto a two-to-three-week computational-physics laboratory module: week one on the Lagrangian derivation and RK4 implementation, week two on phase-space and Poincaré analysis, and (optionally) week three on Lyapunov estimation and a parameter sweep over k_m.

7.2 Broader Significance and Design Implications

Taken on its own, the statement "more damping suppresses chaos" is an expected qualitative result. The contribution we would ask a reader to weigh is narrower and more specific: a quantitative, multi-diagnostic characterization of how fast and through what phase-space route that suppression occurs for a physically grounded, remotely tunable damping mechanism, applied to a system (the double pendulum) that is otherwise a standard chaos benchmark. In engineering terms, the coefficient-to-physics link in Section 3.2 is what would let a designer translate a target damping strength k_m (chosen, e.g., from Table 1, to land in the "moderate" or "strong" regime) into a concrete magnet–conductor specification, in the same spirit as the eddy-current damper design methodology of Polczyński et al. [7] but for a two-body, chaotic mechanical load rather than a single-degree-of-freedom structural mode. We see this translational link, together with the reproducible pedagogical package (Section 7.1), as the most defensible claim to originality in this paper, rather than the qualitative chaos-suppression trend itself.

7.3 Scope, Limitations, and Robustness

We collect the scope limitations of this study explicitly, several of which were raised in review.

Damping model. As discussed in Section 3.3, $\tau_d = -k_m\dot{\theta}$ is the low-velocity, linear limit of eddy-current damping, mathematically equivalent to viscous damping; a nonlinear, velocity-dependent $k_m(\dot{\theta})$ is not modelled. Both joints share one coefficient k_m; independent coefficients $k_{m,1} \neq k_{m,2}$ would be a straightforward but unexplored generalization.

Idealization. The model uses point-mass bobs and neglects arm inertia, air resistance, and bearing friction.

Parameter-sweep sparsity. Only three damping values and a single mass/length/initial-condition configuration are studied. A denser sweep (following the energy-grid approach of Stachowiak and Okada [5]) and a bifurcation diagram in k_m would substantially strengthen the quantitative claims, and are identified as the highest-priority extension of this work.

Lyapunov reliability. Estimates are based on a single 40 s trajectory per damping value with one renormalization protocol (Section 4.3); the sign at $k_m = 0$ should be treated as indicative, not definitive, for the reasons given in Section 6.

No experimental validation. This is an entirely simulation-based study. Physical apparatus of the kind built by Levien and Tan [4], instrumented with a magnetic brake, would be needed to validate the simulated Poincaré sections and energy-decay curves against measurement; none is presented here.

Numerical cross-validation. We have validated the RK4 integrator against itself (time-step halving) and against energy conservation, but not against an independent solver family, as recommended in Section 4.3.

None of these limitations change the qualitative, multi-diagnostic trend of Table 1, but they do bound the precision and generality of the quantitative claims, and we have tried to flag each one at the point in the paper where it is most relevant rather than only here.

8 Conclusion

This paper presented a theoretical and numerical study of a double pendulum under magnetic damping. We derived the coupled equations of motion including a physically motivated eddy-current damping torque, reduced them to a closed-form first-order system, and integrated them with a validated RK4 scheme. Section 2.1 positions this combination of a closed-form damped Lagrangian model, a multi-diagnostic chaos characterization across a damping sweep, and an explicit pedagogical framework relative to the specific prior literature we reviewed, while Section 7.3 lists, without qualification, the respects in which the present study falls short of a fully validated, densely sampled, experimentally confirmed treatment of the system.

The most valuable next steps, in our assessment, are: a fine bifurcation sweep in k_m (rather than three discrete values) to locate the critical damping strength at which chaos is suppressed; longer, ensemble-averaged Lyapunov estimation; a nonlinear, velocity-dependent eddy-current damping law; independent-solver cross-validation; and, most importantly, an experimental benchtop double pendulum with a variable-gap magnetic brake to test the simulated predictions directly, in the spirit of Levien and Tan [4].

A Summary of Numerical Implementation

- **Equations of motion:** closed-form matrix inversion of Section 3.1, evaluated at each RK4 stage.
- **Integration:** fixed-step RK4, $\Delta t = 0.01$ s, $T = 40$ s (validated against $\Delta t = 0.005$ s; Section 4.1).
- **Initial conditions:** $\theta_1 = 120^\circ$, $\theta_2 = -10^\circ$, $\omega_1 = \omega_2 = 0$ (single configuration; see Section 7.3).
- **Damping values studied:** $k_m = 0, 0.05, 0.3$ N·m·s ($\gamma \approx 0, 0.05, 0.3$ in nondimensional units).
- **Poincaré section:** sampled at interpolated $\theta_1 = 0$ crossings (fixed sign of ω_1); θ_2 reduced modulo 2π.
- **Lyapunov estimation:** Benettin-type method, initial separation $\delta_0 = 10^{-10}$ rad, periodic renormalization.
- **Software:** Python 3, NumPy, Matplotlib.

References

[1] S. H. Strogatz. *Nonlinear Dynamics and Chaos: With Applications to Physics, Biology, Chemistry, and Engineering*. (Westview Press, 1994)

[2] F. C. Moon. *Chaotic Vibrations: An Introduction for Applied Scientists and Engineers*. (Wiley, 1992)

[3] T. Shinbrot, C. Grebogi, J. Wisdom, and J. A. Yorke. Chaos in a double pendulum, Am. J. Phys. 60, 491–499 (1993)

[4] R. B. Levien and S. M. Tan. Double pendulum: An experiment in chaos, Am. J. Phys. 61, 1038–1044 (1993)

[5] T. Stachowiak and T. Okada. A numerical analysis of chaos in the double pendulum, Chaos, Solitons & Fractals 29, 417–422 (2006)

[6] J. A. Blackburn, S. Vik, W. Wu, and H. J. T. Smith. Magnetic damping in a pendulum, Am. J. Phys. 63, 833–838 (1995)

[7] K. Polczyński, A. Wijata, J. Awrejcewicz, and G. Niu. Design and dynamic characterization of a large-scale eddy current damper with enhanced performance for vibration control, Mech. Syst. Signal Process. 145, 106879 (2020)

[8] G. Khomeriki. Parametric resonance induced chaos in magnetic damped driven pendulum, Phys. Lett. A 380, 2382–2385 (2016)

[9] M. Hillebrand, S. Zimper, A. Ngapasare, M. Katsanikas, S. Wiggins, and C. Skokos. Quantifying chaos using Lagrangian descriptors, Chaos 32, 123122 (2022)

[10] S. Cabrera, E. D. Leonel, and A. C. Martí. Regular and chaotic phase space fraction in the double pendulum, arXiv:2312.13436 (2023)

[11] E. Ott. *Chaos in Dynamical Systems*, 2nd ed. (Cambridge University Press, 2002)

Reservoir Computing for Time-Series Prediction

Swati Chauhan[1,2], Pratibha Verma[2] and Manish Dev Shrimali[2*]

[1]Graduate School of Engineering, Nagoya Institute of Technology, Nagoya 466 8555, Japan
[2]Department of Physics, Central University of Rajasthan, Ajmer 305 817, India
*shrimali@curaj.ac.in

(Submitted 14-03-2026,
Accepted 09-06-2026)

Abstract

Reservoir computing (RC) is a machine learning framework that utilizes a nonlinear system (often called a reservoir) to process sequential data. In this framework, the reservoir is driven by an input signal, and readouts from the reservoir are trained to generate a desired output signal. Here, we focus on the implementation of the echo state network (ESN) of RC and demonstrate its application for predicting chaotic time series of two representative systems: the Lorenz system and the logistic map. We observe that the ESN framework accurately learns the system's short-term time series while also capturing its long-term dynamical characteristics. We provide a brief overview of the RC framework and illustrate its potential application for time-series forecasting

.

1 Introduction

Today, Artificial Intelligence (AI) is an important field of research, permeating every scientific and technological discipline, while also playing a significant role in our daily lives. Remarkable progress has been made in the field in the last few decades. Notably, machine learning (ML), a key subset of AI, which combines principles from computer science and mathematics, has transformed the idea of how we approach complex problems and harness the power of data effectively. Today, ML is integrated across all areas of technology, affecting any technology user with its applications. For example, advances in ML algorithms have significantly enhanced natural language processing, facilitating the development of powerful language models that are capable of generating human-like text [1], improving web search [2] and powering facial recognition software [3].

Many modern ML applications employ the artificial neural networks (ANNs) framework to process information. Inspired by biological neural networks (BNNs), which represent neural connections in the human brain, ANNs can learn complex relationships across large datasets as they evolve. Due to the availability of ANNs to uncover hidden patterns in data without relying on manually curated features, they are applied over a wide range of applications, ranging from healthcare to agriculture, including speech and image recognition, and time series forecasting [4].

Numerous architectures of ANN have been proposed, which are broadly classified as feedforward neural networks (FNNs) and recurrent neural networks (RNNs). Early applications of NNs often assume that input data samples are independent. While this assumption is valid in many scenarios, these networks restrict results to static, time-independent systems and cannot effectively process sequential data, such as time series or texts. To address these limitations, RNNs were used to capture the temporal dependencies in the data. The feedback mechanism in RNNs enables them to capture information from earlier inputs and maintain it within a hidden state, which can then be utilized for future predictions. Their loop-based architecture allows learning sequential patterns. Despite the remarkable computational power of RNNs for modeling sequential data, the RNNs training process suffers from exploding and vanishing gradients during backpropagation. This limits the network's ability to capture long-term relationships within data. In the early 2000s, fundamentally new approaches to RNNs design were introduced independently by Herbert Jaeger as echo state network (ESN) [5], architecture, which consists of sparsely connected sigmoidal response neurons arranged in a random network architecture. Similarly in the field of computational neuroscience Maass introduced liquid state machines (LSM) [6]. These approaches are collectively referred to as Reservoir Computing (RC) [7]. This study explores the RC paradigm, with particular emphasis on the ESN framework, and evaluates its performance in forecasting nonlinear time-series generated by two prototypical chaotic dynamical systems: the Lorenz system and the logistic map.

Time-series forecasting has been addressed using a wide range of statistical, machine learning, and deep learning approaches. Traditional statistical methods, such as the autoregressive integrated moving average (ARIMA) model, are effective for linear and stationary time series but often struggle to capture the nonlinear characteristics of complex dynamical systems [8]. More recently, deep learning architectures such as long short-term memory (LSTM) networks, gated recurrent units (GRUs), recurrent neural networks (RNNs), and transformer-based models have demonstrated remarkable performance in modeling temporal dependencies and long-range correlations in sequential data [9, 10]. However, these methods typically require extensive training, large datasets, and significant computational resources. In contrast, RC offers an efficient alternative by training only the readout layer while maintaining competitive predictive performance, particularly for nonlinear and chaotic dynamical systems.

2 Reservoir Computing

RC was introduced as a conceptually simple and computationally efficient alternative for training RNNs. RC is specially designed for processing temporal and sequential data generated by dynamical systems. An RC architecture typically consists of three main components: an input layer, a reservoir layer, and an output layer, also called the readout layer. The RC framework uses a fixed, randomly initialized RNN as a reservoir to produce the complex, high-dimensional representations of low-dimensional input data. In general, a reservoir comprises a large network of recurrently coupled units, such as artificial neurons or even a physical dynamical system. The central idea of RC is to simplify the training of RNNs by keeping the input-to-reservoir and reservoir internal connections fixed after random initialization, while only the readout layer is optimized using a regression method. This significantly simplifies the overall training procedure and considerably reduces the computational cost of using the RC method. The simplicity of the training process also reduces the risk of overfitting and mitigates the vanishing and exploding gradient problem present in RNN. During the training phase, the reservoir internal states are recorded at each time step as the input signal drives them. These states collectively form a dynamical features space that encodes the input's history. During prediction phase, a well-trained RC framework no longer requires the external input data. It operates as a dynamical system whose trajectory from a given initial condition represents the predicted temporal evolution of the target system, initialized with the same initial conditions.

Since its development, RC has emerged as a powerful and versatile tool for time-series prediction, often achieving state-of-the-art performance on benchmark datasets. Recently, interest in RC has increased significantly, driven by advances in big data and the growing need for real-time processing [7]. Beyond forecasting, RC frameworks have been applied to hidden variable estimation [11], signal classification [12], learning coupling among oscillators [13, 14], predicting multistability [15], and control engineering [16, 17]. In the context of nonlinear dynamical systems, RC provides an effective approach for analyzing complex temporal behavior, bridging machine learning techniques with the mathematical foundations of dynamical systems theory.

3 Echo state Network

This section introduces the ESN architecture and its training process for time series prediction.

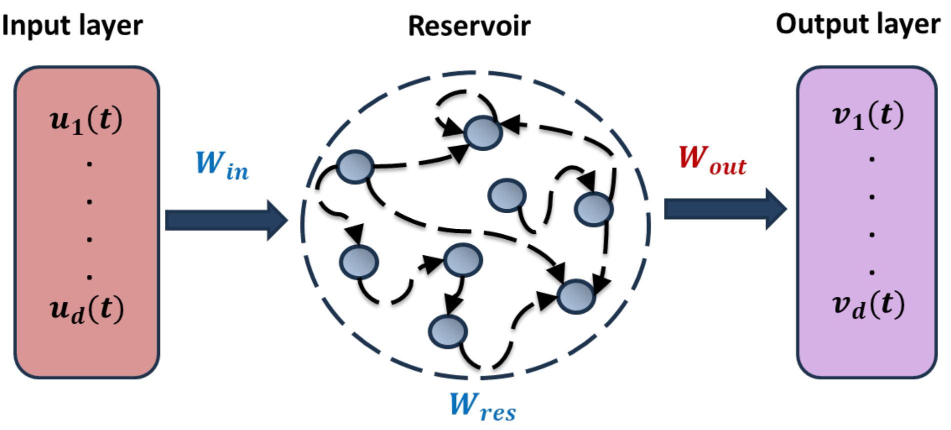

Figure 1: Schematic diagram of echo state network (ESN).

3.1 Architecture

ESN, a prominent RC method, has recently attracted attention for its strong ability to process temporal data [18]. An ESN architecture is composed of three components: an input layer, a reservoir layer, and an output layer. The schematic diagram of the ESN framework is shown in Fig. 1. The (low) d-dimensional input signal is mapped into a (high) N_{res}-dimensional space through the weighted $N_{res} \times d$ matrix $\mathbf{W_{in}}$, often referred to as the input connection matrix. The reservoir layer is composed of a network of N_{res} neurons, characterized by $\mathbf{W_{res}}$, an adjacency matrix of dimension $N_{res} \times N_{res}$. The N_{res}-dimensional signal from the reservoir layer is mapped back into the lower-dimensional output signal via the output weighted matrix $\mathbf{W_{out}}$.

The internal dynamics of the reservoir evolve according to the nonlinear state update equation:

$$\mathbf{r}(t+1) = (1-\alpha)\mathbf{r}(t) + \alpha\mathbf{F}\left(\mathbf{W_{res}}\mathbf{r}(t) + \mathbf{W_{in}}\mathbf{u}(t)\right) \quad (1)$$

Here, $\mathbf{r}(t) \in \mathbb{R}^{N_{\text{res}}}$ is a column vector that represents the reservoir states at time t, and $\mathbf{u}(t) \in \mathbb{R}^d$ is the input data. Here $\mathbf{F}$ is the activation function that introduces non-linearity, allowing the reservoir to capture complex temporal patterns.

Training phase : During the training phase, the reservoir layer is excited with input data $\mathbf{u}(t)$ for a time length from $t=0$ to $t = T_{train}$, where T_{train} is the number of data points in the training set. The internal states of the reservoir $\mathbf{r}(t)$ are calculated at each time step using Eq. 1. The column vector $\mathbf{r}(t)$ is collected at each time step and is stored in a reservoir matrix $\mathbf{R}$ after discarding a few transient time steps T_{trans}. Thus $\mathbf{R}$ is a matrix of dimension $N_{res} \times (T_{train} - T_{trans})$. Notably, the initial state of column vector $\mathbf{r}(t)$ is set as 0. The target data corresponding to the input signal is also collected in a $\mathbf{T_{teach}}$ over the same training length after discarding the transient time steps. Now the objective is to determine the weights in the readout layer $\mathbf{W_{out}}$ such that

$$\mathbf{v}(t) = \mathbf{W_{out}}\mathbf{r}(\mathbf{t}) \tag{2}$$

here $\mathbf{v}(t) \in \mathbb{R}^d$ is the predicted output vector. The weights of $\mathbf{W_{out}}$ are obtained to minimize the difference between $\mathbf{T_{teach}}$-$\mathbf{W_{out}}\mathbf{r}(t) \approx 0$. We apply ridge regression and calculate the weights of the readout layer using the expression:

$$\mathbf{W}_{out} = \mathbf{T}_{teach}\mathbf{R}\left[\mathbf{R}^T\mathbf{R} + \beta I\right]^{-1} \tag{3}$$

where β is the regularization parameter and I is the identity matrix.

Prediction phase : During prediction phase the reservoir states $\mathbf{r}(t)$ are updated using Eq. 1. The reservoir states are collected after discarding a warmup time steps and are used to calculate output $\mathbf{v}(\mathbf{t})$ using Eq. 2. The only difference during prediction from training is that now the network operates autonomously such that the predicted output is used as the input in Eq. 1, i.e., $\mathbf{u}(\mathbf{t+1}) = \mathbf{v}(\mathbf{t})$.

3.2 Generation of Matrices

As seen in the previous section, during the ESN training process, the input and reservoir weight matrices, $\mathbf{W_{in}}$ and $\mathbf{W_{res}}$, are randomly initialized. We first discuss the generation of random matrix $\mathbf{W}_{res} \in \mathbb{R}^{N_{res}\times N_{res}}$.

- The reservoir weight matrix $\mathbf{W_{res}}$ is constructed by first generating an initial matrix $\mathbf{W_0} \in \mathbb{R}^{N_{res}\times N_{res}}$ that represents the connectivity between the nodes of the reservoir.
- The entries of $\mathbf{W}_0$ are assigned random weights with a specified connection probability p.
- Next, the maximum absolute eigenvalue of $\mathbf{W_0}$, denoted as ρ_0, is computed.
- Finally, the matrix is rescaled as $\mathbf{W_{res}} = \frac{\rho}{\rho_0}\mathbf{W_0}$, ensuring that the largest absolute eigenvalue of the matrix $\mathbf{W_{res}}$ is ρ.

Next, the input weight matrix $\mathbf{W_{in}} \in \mathbb{R}^{N_{res}\times d}$ is generated such that the nonzero elements of $\mathbf{W_{in}}$ are sampled from a uniform distribution in the interval $[-\sigma, \sigma]$. In each column of $\mathbf{W_{in}}$, N_{res}/d elements are chosen to be nonzero in such a way that each reservoir node receives input from only one variable of the input vector.

3.3 Hyperparameters Optimization

The ESN architecture involves several hyperparameters, including the spectral radius ρ, the link probability p governing the reservoir network's connectivity, the scaling factor of the input weight matrix σ, the leakage parameter α, and the regularization coefficient β. These hyperparameters are selected before training and remain fixed throughout the learning process. The values of these hyperparameters significantly affect the predicted output; therefore, optimizing them before making predictions is crucial. For instance, the reservoir size, or the number of neurons in the reservoir layer N_{res}, can be viewed as a proxy for the computational resources allocated to the task. In general, increasing N_{res} tends to improve the performance of the ESN scheme. Similarly, α, the leakage parameter, defines the reservoir's characteristic time scale. The spectral radius ρ affects the memory of the reservoir. There are several optimization strategies, such as grid search, random search, Bayesian optimization [19], and so on.

4 Time Series Prediction

To demonstrate the effectiveness of ESN for processing temporal data, we consider time-series prediction of the Lorenz system and the logistic map as representative examples. We aim to predict the time series of both the Lorenz system and the logistic map in their chaotic regimes. The sensitive dependence of these systems on initial conditions makes it difficult to accurately predict their trajectories for long time intervals in a chaotic regime [20]. Here, we focus on predicting time series at short time steps while reproducing the attractor over longer times.

4.1 Lorenz system

The Lorenz system is one of the most well-known chaotic systems in nonlinear dynamics. It was originally introduced by Edward Lorenz while studying atmospheric convection [21]. The extreme sensitivity of the system to its initial condition gives rise to the well-known concept of the butterfly effect, where even small differences at the start can lead to significantly different trajectories over time. The Lorenz system is governed by the following set of ordinary differential equations

$$\begin{aligned}\frac{dx}{dt} &= \sigma_l(y-x),\\ \frac{dy}{dt} &= x(\rho_l - z) - y,\\ \frac{dz}{dt} &= xy - \beta_l z,\end{aligned} \tag{4}$$

where σ_l, ρ_l, and β_l are system parameters. In a chaotic regime, the commonly used parameter values in the Lorenz system are $\sigma_l = 10$, $\rho_l = 28$, and $\beta_l = 8/3$. The Lorenz system in Eq. (4) is numerically integrated using the fourth-order Runge–Kutta method with time step of $dt = 0.01$. The original time series of the variables (x, y, z) of the Lorenz system are shown in Fig. 2 as a solid line (blue). The corresponding phase space in (x, z) plane is also plotted in Fig. 3 using a solid line (blue).

In order to predict the time series of the Lorenz system, we use the ESN architecture. The input data, consisting of the Lorenz system variables $u(t) = [(x(t), y(t), z(t))]$, is sequentially fed into the reservoir for $T_{train} = 50000$ time steps. At each training step, the reservoir state is updated using Eq. 1, and the resulting reservoir states are collected in the reservoir matrix $\mathbf{R}$ after discarding a few transient steps ($T_{trans} = 100$). The complete training procedure of the ESN is described in Sec. 3. The corresponding target

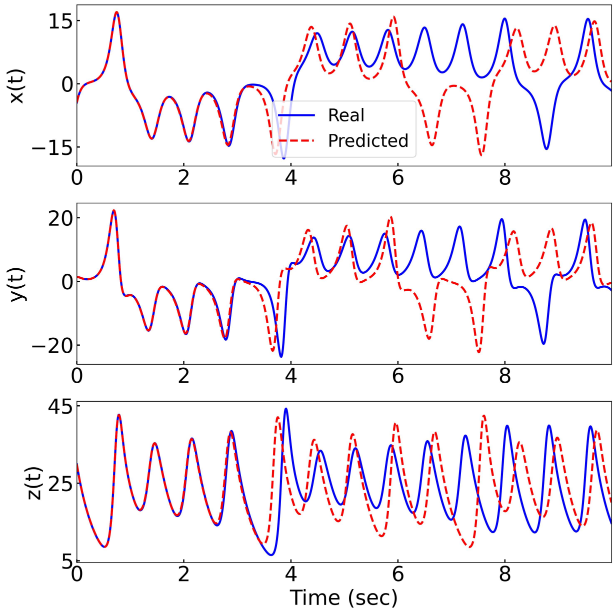

Figure 2: Time series of real (solid blue line) and predicted (dashed red line) Lorenz system variables.

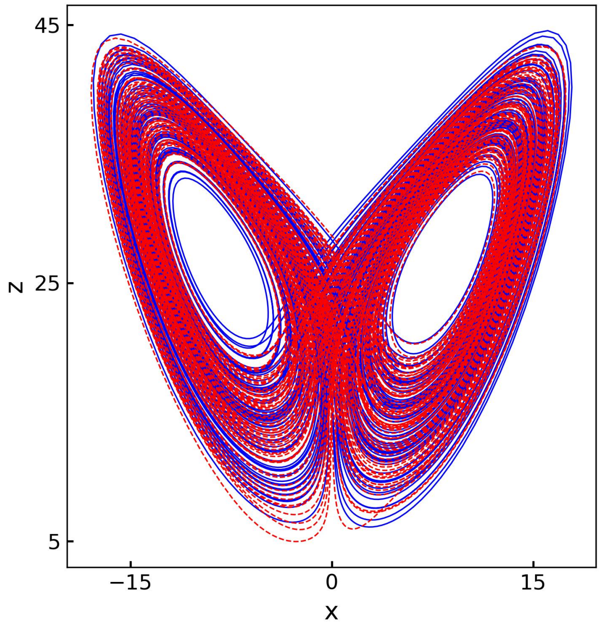

Figure 3: Phase portrait of real (solid blue line) and predicted (dashed red line) Lorenz attractor.

data is also collected in the matrix $\mathbf{T_{teach}}$ over the same training interval after discarding the transient. The readout weights $\mathbf{W}_{out}$ are then optimized. Once the training is completed, the trained reservoir is used to predict the target output $\mathbf{v(t)}$ using Eq. 2. This predicted output vector $\mathbf{v(t)}$, consisting of the predicted state variables of the Lorenz system, is then fed back into the reservoir as the next input, enabling the reservoir to generate future time-series values autonomously. The predicted and original time series of the Lorenz system are presented in Fig. 2. Fig. 3 shows the predicted and original phase space of the chaotic Lorenz attractor. We observe that the short-term predictions are highly accurate, while the system's long-term behavior remains well-preserved. The hyperparameters for this case are [$N_{res} = 500$, $\alpha = 0.75$, $\rho = 0.8$, $p = 50$, $\sigma = 0.27$, $\beta = 0.01$].

4.2 Logistic map

The Logistic map is one of the simplest and most widely studied discrete-time chaotic systems in nonlinear dynamics. It was originally introduced as a mathematical model for population growth [22]. The logistic map is defined by the following nonlinear difference equation

$$x(t+1) = ax(t)(1 - x(t)), \tag{5}$$

where $x(t)$ represents the state variable at discrete time step t, and a is the control parameter that determines the dynamical be-

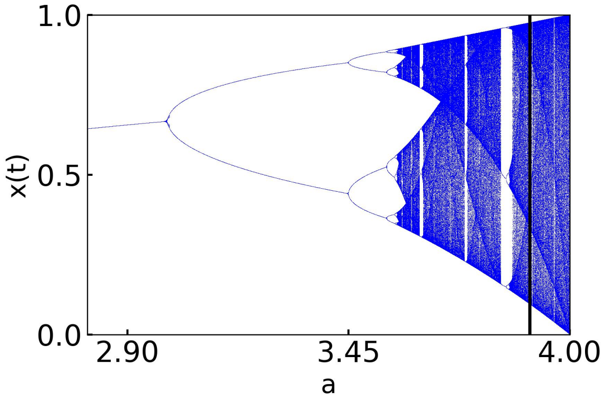

Figure 4: The bifurcation diagram of the logistic map. The solid black vertical line indicates the parameter value $a = 3.9$.

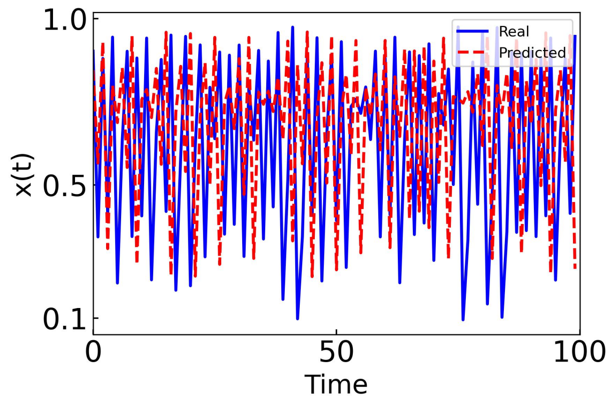

Figure 5: Time series of real (solid blue line) and predicted (dashed red line) logistic map.

havior of the system. The time series of the logistic map is generated using Eq. 5 starting from an initial condition $x(0)$. The original bifurcation diagram for parameter values $a \in [2.8, 4.0]$ is plotted in Fig. 4, illustrating the well-known period-doubling behavior. For certain parameter values, such as $a = 3.9$, the system exhibits chaotic dynamics, as indicated by the vertical solid black line in Fig. 4. The corresponding time series $(x(1), x(2), x(3), \ldots, x(t))$ at $a = 3.9$ generated from an initial condition $x(0)$ is plotted in Fig. 5 using a solid line (blue).

We now employ the ESN architecture to predict the time series of the logistic map. The input data consists of the state variable of the logistic map $\mathbf{u}(\mathbf{t}) = [x(t)]$, is sequentially fed into the reservoir for $T_{train} = 50000$ times steps. At each training step, the reservoir state is updated using Eq. 1, and the resulting reservoir states are collected after discarding $T_{trans} = 100$ time steps. The corresponding target data is also collected in the matrix $\mathbf{T_{teach}}$ over the same training interval after discarding the transient. Once the training process is completed, the optimized readout weights $\mathbf{W_{out}}$ are used for prediction. During the prediction phase, the predicted output vector $\mathbf{v}(\mathbf{t})$, consisting of the state variable of the logistic map $(x(t))$, is fed back into the reservoir as the next input, allowing the reservoir to autonomously generate future time-series values of the logistic map. The predicted and original time series of the logistic map are presented in Fig. 5. The hyperparameters for this case are $[N_{res} = 200$, $\alpha = 1.0$, $\rho = 0.8$, $p = 50$, $\sigma = 0.27$, $\beta = 0.01]$.

5 Conclusion

This study presents a pedagogical introduction to ML where the fundamental concepts of RC are introduced, an ML framework, with particular emphasis on the ESN architecture. The work explains the structure of

ESN and the training procedure. To demonstrate the approach's effectiveness in predicting sequential data, a time-series prediction task is performed on two chaotic systems: the Lorenz system and the logistic map. We show that ESN can accurately predict short-term behavior while preserving the long-term dynamics of the systems. The ESN algorithm for time series prediction is also provided in the appendix Sec. 6.

Recently, there has been an increasing interest in incorporating physical knowledge of the system into ML architectures to improve prediction accuracy. Such frameworks are commonly referred to as physics-informed neural networks (PINNs). Motivated by this concept, the prediction capabilities of the standard RC approach can also be enhanced by incorporating a physics-informed model. This approach is referred to as physics-informed RC (PIRC) [23, 24]. In addition, another branch of RC has recently gained significant attention, as it leverages the physical properties and dynamics of a system as a computational substrate. This approach is known as physical RC (PRC) [25, 26]. Given the rapid growth of ML, this work offers a clear, accessible introduction to applying ML techniques to time series prediction.

6 Appendix

ESN algorithm for time-series prediction.

1: **Input data:** Collect training data $\mathbf{u}(\mathbf{t})$ for $t = 1 - T_{train}$ from model system.

2: Generate $\mathbf{W_{in}} \in \mathbb{R}^{N_{res} \times d}$

3: Generate $\mathbf{W_{res}} \in \mathbb{R}^{N_{res} \times N_{res}}$

4: **Training phase**

for $t = 1$ to T_{train}

$\mathbf{r}(t) = (1-\alpha)\mathbf{r}(t-1) + \alpha \tanh(\mathbf{W_{res}}\mathbf{r}(t-1) + \mathbf{W_{in}}\mathbf{u}(\mathbf{t}))$

store $\mathbf{r}(t)$ in matrix $\mathbf{R}$

end for

5: Construct teacher matrix $\mathbf{T_{teach}}$ that contains target signal

6: **Learning readout layer weights** : $\mathbf{W_{out}} = \mathbf{T_{teach}}\mathbf{R}(\mathbf{R}^T\mathbf{R} + \beta I)^{-1}$

7: **Prediction phase**

Put $\mathbf{u}(\mathbf{t}) = \mathbf{u}(\mathbf{T_{train}})$ and run reservoir

for $t = 1$ to T_{pred}

$\mathbf{r}(t) = (1-\alpha)\mathbf{r}(t-1) + \alpha \tanh(\mathbf{W_{res}}\mathbf{r}(t-1) + \mathbf{W_{in}}\mathbf{v}(\mathbf{t}))$

where $\mathbf{v}(\mathbf{t}) = \mathbf{W_{out}}\mathbf{r}(t)$

end for

Code Availability

The Python implementation of the ESN framework presented in this work is openly available at `https://github.com/2024phdphy004-bot/Reservoir-Computing-for-Time-Series-Prediction.git` to facilitate reproducibility and further research.

References

[1] Devlin, J., Chang, M., Lee, K. & Toutanova, K. Bert: Pre-training of deep bidirectional transformers for language understanding. *Proceedings Of The 2019 Conference Of The North American Chapter Of The Association For Computational Linguistics: Human Language Technologies, Volume 1 (long And Short Papers)*. pp. 4171-4186 (2019)

[2] Guo, X., Singh, S., Lee, H., Lewis, R. & Wang, X. Deep learning for real-time Atari game play using offline Monte-Carlo tree search planning. *Advances In Neural Information Processing Systems*. **27**, pp. 3338 - 3346 (2014)

[3] Brunelli, R. & Poggio, T. Face recognition: Features versus templates. *IEEE Transactions On Pattern Analysis And Machine Intelligence*. **15**, 1042-1052 (1993)

[4] Lim, B. & Zohren, S. Time-series forecasting with deep learning: a survey. *Philosophical Transactions Of The Royal Society A: Mathematical, Physical And Engineering Sciences*. **379**, 2194 (2021)

[5] Jaeger, H. The "echo state" approach to analysing and training recurrent neural networks-with an erratum note. *Bonn, Germany: German National Research Center For Information Technology Gmd Technical Report*. **148**, 13 (2001)

[6] Maass, W., Natschläger, T. & Markram, H. Real-time computing without stable states: A new framework for neural computation based on perturbations. *Neural Computation*. **14**, 2531-2560 (2002)

[7] Tanaka, G., Yamane, T., Héroux, J., Nakane, R., Kanazawa, N., Takeda, S., Numata, H., Nakano, D. & Hirose, A. Recent advances in physical reservoir computing: A review. *Neural Networks*. **115**, 100–123 (2019).

[8] Tunnicliffe Wilson, G. Time Series Analysis: Forecasting and Control, 5th Edition, by George E. P. Box, Gwilym M. Jenkins, Gregory C. Reinsel and Greta M. Ljung. *Journal of Time Series Analysis*. **37**, 286–287 (2016).

[9] Vaswani, A., Shazeer, N., Parmar, N., Uszkoreit, J., Jones, L., Gomez, A. N., Kaiser, L. & Polosukhin, I. Attention Is All You Need. In *Advances in Neural Information Processing Systems (NeurIPS)*, pp. 5998–6008 (2017).

[10] Lu, G., Ou, Y., Wang, Z., Qu, Y., Xia, Y., Tang, D., Kotenko, I. & Li, W. A Survey of Deep Learning for Time Series Forecasting: Theories, Datasets, and State-of-the-Art Techniques. *Computers, Materials and Continua*. **85**(2), 2403–2441 (2025).

[11] Lu, Z., Pathak, J., Hunt, B., Girvan, M., Brockett, R. & Ott, E. Reservoir

observers: Model-free inference of unmeasured variables in chaotic systems. *Chaos: An Interdisciplinary Journal Of Nonlinear Science*. **27**, 041102 (2017)

[12] Carroll, T. Using reservoir computers to distinguish chaotic signals. *Physical Review E*. **98**, 052209 (2018)

[13] Mandal, S. & Shrimali, M. Learning unidirectional coupling using an echo-state network. *Physical Review E*. **107**, 064205 (2023)

[14] Chauhan, S., Mandal, S., Dixit, S. & Dev Shrimali, M. Predicting collective states of a star network using reservoir computing. *Chaos: An Interdisciplinary Journal Of Nonlinear Science*. **35**, 123112 (2025)

[15] Roy, M., Mandal, S., Hens, C., Prasad, A., Kuznetsov, N. & Dev Shrimali, M. Model-free prediction of multistability using echo state network. *Chaos: An Interdisciplinary Journal Of Nonlinear Science*. **32**, 101104 (2022)

[16] Waegeman, T., Schrauwen, B. & Others Feedback control by online learning an inverse model. *IEEE Transactions On Neural Networks And Learning Systems*. **23**, 1637-1648 (2012)

[17] Mandal, S., Chauhan, S., Verma, U., Shrimali, M. & Aihara, K. Adaptive control of dynamical systems using reservoir computing. *Chaos: An Interdisciplinary Journal Of Nonlinear Science*. **35**, 091102 (2025)

[18] Lukoševičius, M. & Jaeger, H. Reservoir computing approaches to recurrent neural network training. *Computer Science Review*. **3**, 127–149 (2009).

[19] Yperman, J. & Becker, T. Bayesian optimization of hyper-parameters in reservoir computing. *ArXiv Preprint ArXiv:1611.05193*. (2016)

[20] Pathak, J., Wikner, A., Fussell, R., Chandra, S., Hunt, B., Girvan, M. & Ott, E. Using machine learning to replicate chaotic attractors and calculate Lyapunov exponents from data. *Chaos: An Interdisciplinary Journal Of Nonlinear Science*. **28**, 041101 (2018).

[21] Lorenz, Edward Norton "Deterministic nonperiodic flow," *Journal of the Atmospheric Sciences*, **20**(2), pp. 130–141, 1963.

[22] R. M. May, "Simple mathematical models with very complicated dynamics," *Nature*, **261**(5560), pp. 459–467, 1976.

[23] Mammedov, Y., Olugu, E. & Farah, G. Weather forecasting based on data-driven and physics-informed reservoir computing models. *Environmental Science And Pollution Research*. **29**, 24131-24144 (2022)

[24] Perrusquía, A. & Guo, W. Reservoir computing for drone trajectory intent prediction: A physics informed approach. *IEEE Transactions On Cybernetics*. **54**, 4939-4948 (2024)

[25] Nakajima, K. Physical reservoir computing—an introductory perspective. *Japanese Journal Of Applied Physics*. **59**, 060501 (2020)

[26] Mandal, S., Sinha, S. & Shrimali, M. Machine-learning potential of a single pendulum. *Physical Review E*. **105**, 054203 (2022).